UNIVERSITÀ DEGLI STUDI DI GENOVA

SCUOLA POLITECNICA

DIME

Dipartimento di Ingegneria Meccanica, Energetica, Gestionale e dei Trasporti

TESI DI LAUREA

IN

INGEGNERIA MECCANICA-ENERGIA E AERONAUTICA

Riduzione della resistenza legato all'utilizzo delle superfici superidrofobiche

Relatore:
Chiar.mo Prof. Ing. Alessandro Bottaro
Chiar.mo Prof. Ing. Nicolas Mazellier

Allievo: Sofia Pavese

Anno scolastico 2023/2024

Sommario

Questo studio mira a valutare gli effetti dei rivestimenti superidrofobici sulla riduzione della resistenza, soprattutto nelle applicazioni marine, al fine di minimizzare in modo significativo l'attrito e, di conseguenza, il consumo di carburante. Basandosi sulla ricerca precedente di Castagna, il presente lavoro adotta un approccio utilizzando un corpo cilindrico anziché una sfera, motivato dalla limitazione di quest'ultima nel permettere un'analisi agevole della deformazione dello strato d'aria, aspetto di notevole interesse. Per la costruzione dei cilindri, è stata impiegata una stampante 3D per controllare tutti i parametri superficiali, mentre internamente è stata inserita una barra di acciaio per aumentarne il peso. I test sperimentali hanno coinvolto la caduta libera dei cilindri all'interno di una tanica. Al fine di evitare collisioni con le pareti e qualsiasi movimento di inclinazione, sono stati aggiunti due dischi agli estremi del cilindro. L'analisi post-processing mediante cross-correlazione ha evidenziato una riduzione della resistenza, con particolare influenza della distanza λ tra due pilli. Questi risultati promettenti per la ricerca futura in ambito marittimo evidenziano, tuttavia, che siamo ancora lontani dall'applicazione pratica diretta.

Abstract

This study aims to evaluate the effects of superhydrophobic coatings on reducing resistance, particularly in marine applications, with the goal of significantly minimizing friction and consequently fuel consumption. Building upon Castagna's previous research, this work adopts an approach using a cylindrical body instead of a sphere, motivated by the latter's limitation in allowing for easy analysis of air layer deformation, a highly interesting aspect.

For the construction of the cylinders, a 3D printer was used to control all surface parameters, while internally, a steel bar was inserted to increase their weight. Experimental tests involved the free fall of the cylinders inside a tank. In order to avoid collisions with the walls and any tilting movement, two disks were added to the two ends of the cylinder. Post-processing analysis through cross-

correlation revealed a reduction in resistance, with particular influence from the distance λ between two pillars. These promising results for future research in maritime applications highlight, however, that we are still far from direct practical application.

Sommario

1. Introduction

In the contemporary era, a critical concern revolves around the imperative to curtail fluid consumption in response to the escalating prevalence of air pollution. This objective can be realized through fuel modification or the mitigation of drag. Engineers are currently engrossed in the examination of a distinct type of surface denoted as superhydrophobic surface (SH), endeavouring to achieve drag reduction in liquid environments. This surface exhibits diverse applications, spanning both military and civilian domains.

Within military contexts, submarines stand to gain substantial advantages from SH surfaces. These surfaces engender a reduction in vulnerability by augmenting the maximum velocity and enhancing the target direction of submarines. Furthermore, submarines equipped with SH surfaces manifest heightened manoeuvrability, control, and hydrodynamic performance, leading to a concomitant diminution in fuel costs under typical operational conditions.

Moreover, SH surfaces present potential applications in the realm of civilian transport. In operational conditions, skin friction contributes approximately 50% of the total drag for long-range aircraft during cruise conditions. This contribution escalates to approximately 85% for low-speed cargo ships and constitutes the predominant share of drag in oil transport pipelines. The envisaged reduction in drag holds the potential to engender amplified vehicle speed at constant power or diminished power requisites at a constant speed, thereby exerting a potential influence on global greenhouse gas emissions and contributing to sustainable development.

The properties of SH surfaces have garnered substantial attention since the 1990s, with their most noteworthy attribute being drag reduction. In essence, drag can be partitioned into two principal components: skin friction, associated with the interaction of the boundary layer with the surface along the entire body length, and pressure drag, correlated with the pressure difference between the front and rear sides of the body. The latter is primarily attributed to the wake developing behind the body and is contingent on the body's shape. For instance, streamlined shapes like airfoils at low angles of attack can minimize pressure drag. The interrelation between these two contributions can be visualized on an airfoil by examining their dependence on the aspect ratio (Figure 1.1).
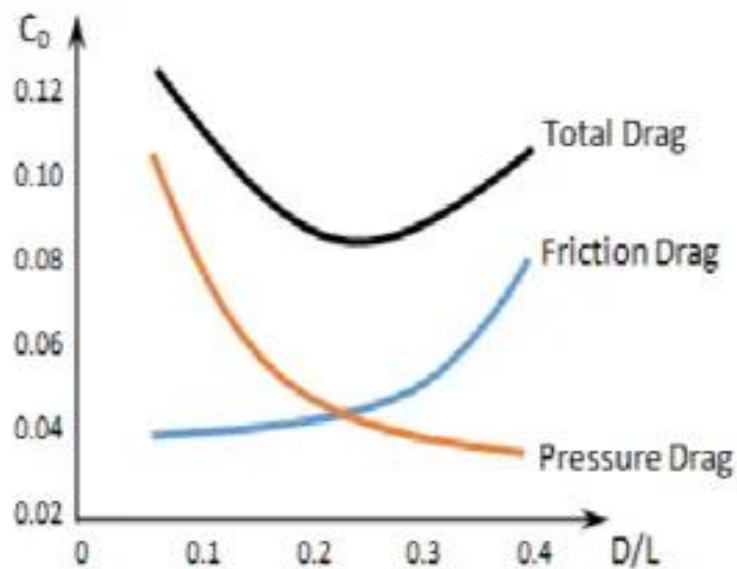
Figure 1-1 Evolution of the total drag, togheter with the pressure and viscous contiubution, as function of the body length over a diameter ratio (web)

The superhydrophobic surface primarily influences the first contribution, specifically reducing skin friction. To comprehend this phenomenon, it is crucial to examine the region in close proximity to the wall, known as the boundary layer. In this zone, there is a significant velocity variation across a confined height perpendicular to the surface, resulting in the predominance of viscous forces. This physical occurrence arises from the impossibility of having a discontinuity between local free stream and body velocities; for standard surfaces, the relative velocity between the flow and the wall must be zero.

For superhydrophobic surfaces, the situation deviates slightly. The surface can trap air within its roughness, thereby reducing the contact area between the liquid and solid. This characteristic introduces slippage. The slip boundary condition, initially proposed by Navier, is illustrated in Figure 1.2. In Navier's model, the velocity at the liquid/gas interface is not zero, but a measurable slip velocity is present, proportional to the shear rate experienced by the fluid at the wall. This mechanism leads to a reduction in skin friction.

The slip velocity is a very important parameters for the reduction of drag and it is defined as:

$$u_0 = b * \left| \frac{\partial u}{\partial y} \right|$$

(1.1)

Where b is the slip length, a parameter which is correlated with the dimension of the roughness of the surface, and it is very difficult to compute or measure, as we will see in chapter 3.3.
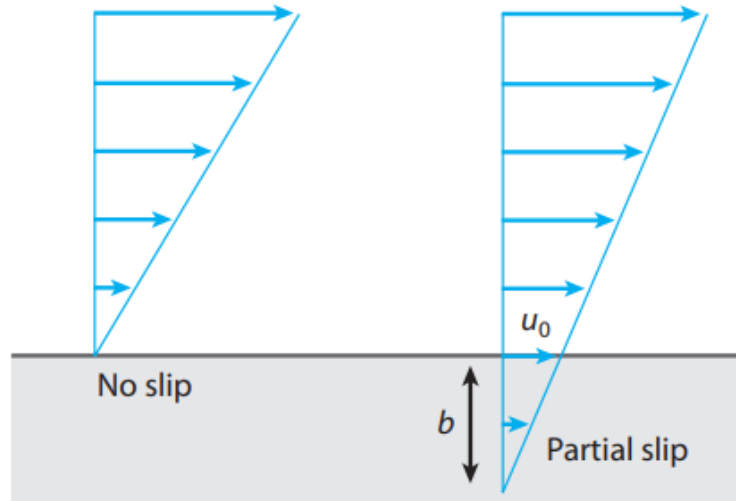

Figure 1-2 Schematic diagram of slip at a fluid-solid interface [Jonathan P. Rothstein (2009)]

As mentioned earlier, one of the key features of the superhydrophobic surface is its roughness, which can be either natural, as seen in lotus leaves (figure 1.3 and 1.4) that inspired engineers in developing this surface, or artificial. Another crucial characteristic is the chemical properties. Given that this surface is utilized with water or a mixture of water and another liquid, such as glycerine, it is essential that the material is composed of non-polar molecules and exhibits lower surface energy. Further exploration of these surface characteristics will be detailed in Chapter 3.1.
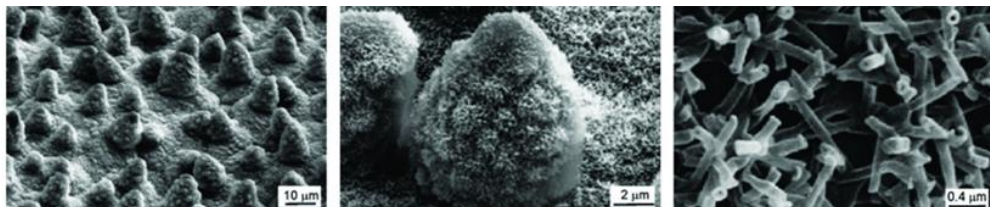

Figure 1-3 Three different magnification of SEM images showing morphological micro- and nanostructures. Koch et al (2009).

Figure 1-4 Water droplet beading on lotus leaf with static contact angle higher than 150 degrees. [web]

The objective of this thesis is to extend the investigation initiated by Marco Castagna (2019) by quantifying the drag reduction on a falling cylinder submerged in a tank filled with pure water. The methodology involves conducting an experimental campaign to gather relevant data, in particular sequence of photographs. Subsequently, an analysis is performed to extract velocity and position information, allowing for the determination of drag forces.

Let's now analysed in detail the concepts mentioned above.

1.1.   Super-hydrophobic surface

1.1.1.   Slip model

For the classical surface the no-slip condition is accepted almost universally: in particular if we analysed the region very close to the surface, the boundary layer, the relative velocity between flow must be zero at the wall This is physically due to the fact that a discontinuity between a local free stream and body velocities cannot exist. The validity of the no slip boundary condition was debated quite extensively throughout the nineteenth century. In the end, its implementation arose from a wealth of experimental validation. This model, however, is not valid for superhydrophobic surfaces. where it is introduced the model of slip condition. For the super hydrophobic surface, the surface can entrap a gas layer in their roughness (the roughness distinguishes hydrophobic from superhydrophobic surface) reducing the liquid/solid contact area as show in figure 1.5.
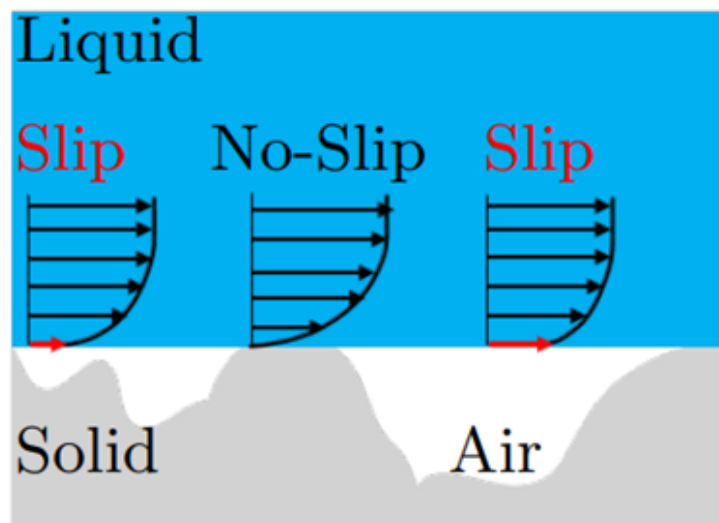

Figure 1-5 Schematic rappresentation of the slip condition on a randomic roughness surface

N. Bettaieb (2022)

This feature yield slippage. The concept of slip boundary condition was first proposed by Navier and is shown in figure 1.6. As we can see in this model, we do not consider the two different conditions of slip and no-slip as before, but we consider a homogenous slip. In Navier's model, the velocity at the interfaces liquid/gas is not zero so it is possible to measure a slip velocity proportional to the magnitude of the shear rate experienced by the fluid at the wall and this leads to a skin friction reduction. The slip boundary condition, originally proposed by Navier (1823) in 1823, as introduced before, posits that the slip velocity (u_0) is

directly proportional to the shear rate experienced by the fluid at the solid-fluid interface, given by:

$$u_0 = b * \left|\frac{\partial u}{\partial y}\right| \qquad \text{where b represents the slip length.} \qquad (1.2)$$
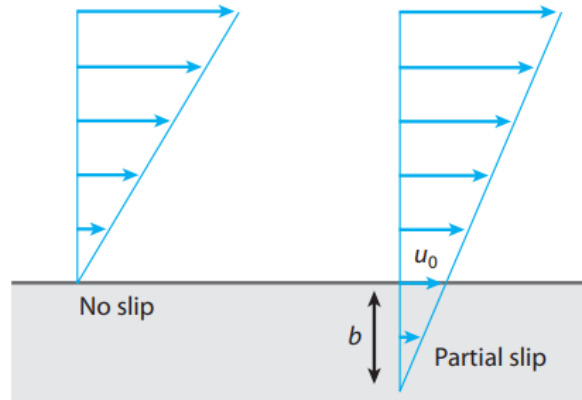

Figure 1-6 Schematic diagram of no slip at a fluid-solid interface and a homogenisation condition of partial slip on a superhydrophobic surface

[Jonathan P. Rothstein (2009)]

The first study on this type of surface highlights the effect of the slip on the reduction of the drag, due to the reduction of skin-friction but also due to the variation of the separation angle. So, an important parameter to evaluate is the slip length link to the slip velocity.

Recent investigations have primarily focused on determining the magnitude of the slip length and its dependency on factors such as wettability and surface roughness (Lauga et al. 2007, Vinogradova 1999)

1.1.2. Technique for the measure of the slip length

A challenge for lot of years is how to measure directly the slip length: in particular lot of scientists try to find which method is more precise for the direct measurement. Recent advancements have overcome experimental challenges, enabling consistent measurements across various techniques.

The first trying is the molecular dynamic simulations conducted by Thompson & Troian (1997) and Barrat & Bocquet (1999) provided early insights into the potential of surface hydrophobicity to generate slip lengths significantly larger than the mean free path.

Several studies have determined slip lengths through pressure-drop measurements (Choi et al. 2003, Schnell 1956) or friction-factor measurements (Baudry et al. 2001; Cottin-Bizonne et al. 2005; Zhu & Granick 2001, 2002) using simple fluids flowing over nonwetting smooth surfaces. Cottin-Bizzone and colleagues (2005) employed a periodic squeezing flow with nanometre-sized oscillations to measure hydrodynamic forces and calculate the resulting slip length. In their experiments, hydrophobic surfaces exhibited slip lengths of approximately b ≈ 20 nm, while hydrophilic surfaces had no measurable slip length. These surfaces had an RMS roughness of approximately 1 nm. Similar measurements with other surfaces showed that the maximum slip length corresponded to the surfaces with the smallest RMS roughness (Zhu & Granick 2002).

Direct measurements of slip velocity at or near the wall over smooth hydrophobic surfaces are limited due to the small slip lengths and velocities (Jin et al. 2004, Joly et al. 2006, Joseph & Tabeling 2005, Pit et al. 1999). Joseph & Tabeling (2005), using micro-particle image velocimetry (μ-PIV), found a slip length of approximately b ≈ 30 nm for water flow through a microchannel coated with a monolayer of hydrophobic octadecyltrichlorosilane. However, similar to earlier μ-PIV experiments measuring larger slip lengths (Tretheway & Meinhart 2002), the measured slip length values were within the error of velocity measurements. Pit et al. (1999) utilized total internal reflection fluorescence microscopy (TIRF) to measure slip velocity of hexadecane past an iyophobically modified smooth sapphire surface, obtaining slip lengths of approximately b ≈ 20 nm. Recent advancements in μ-PIV have reduced measurement errors and typical slip length values. Jin et al. (2004) combined TIRF with particle tracking velocimetry (PTV) to measure the velocity of water near a glass surface coated with a self-assembled monolayer of OTS, yielding slip lengths less than b < 10 nm. Their measurements revealed features affecting previous μ-PIV and PTV, including non-Gaussian Brownian motion and hindered diffusion near the wall due to lubrication effects.

Nevertheless, throughout this campaign, none of these methods were employed; instead, a global estimation of the drag coefficient was conducted in fact Samaha et al. (2011) find a link between the slip length and drag reduction (if the slip length increases also the drag reduction increase). The experimental aspects, such as those undertaken during the internship and other related activities, become crucial in this context. Before delving into the measurement procedure for the drag coefficient, it is paramount to characterize the surface.

1.1.3. Hydrophobicity measure

In this section we are going to characterise the wettability of a solid surface to understand the characteristics of the superhydrophobic surface.

The most commonly utilized parameter for describing the wetting behaviour of a solid substrate is the contact angle ϑ_s, defined as the angle formed between a liquid drop and a solid surface. A surface is categorized as hydrophilic if $0° \leq \vartheta_s \leq 90°$, indicating that water

easily wets the solid (Bhushan & Jung, 2011). Hydrophilic materials constitute a significant portion of naturally occurring substances.

Conversely, when $91° \leq \vartheta_s \leq 180°$ the solid surface is deemed hydrophobic. The upper limit of 180° corresponds to a perfectly spherical drop in contact with the solid surface. Two additional sub-ranges can be defined: for $\vartheta_s \leq 10$ the strong affinity between the solid material and water characterizes the material as super-hydrophilic; on the other hand, when $150° \leq \vartheta_s \leq 180$ the material is termed superhydrophobic (as shown in figure 1.7).
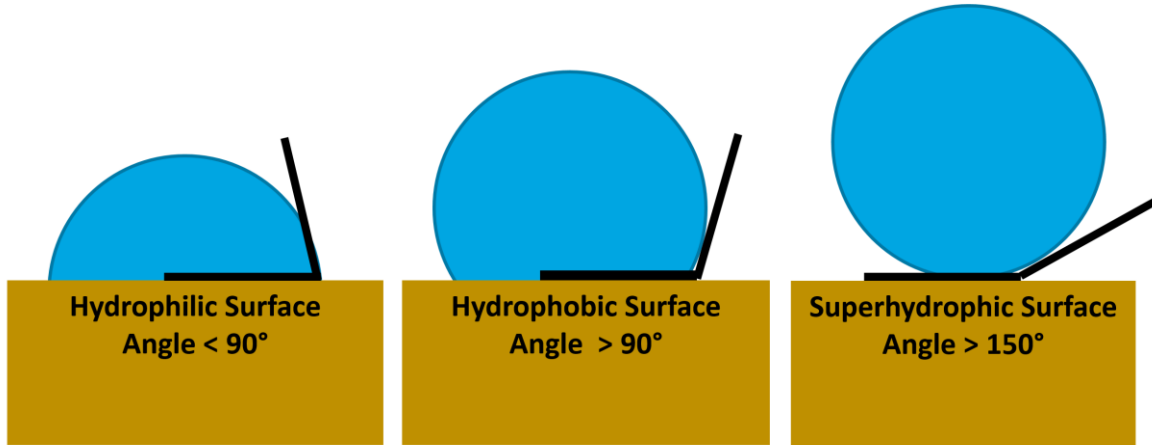

Figure 1-7 Definition of the macroscopic static contact angle on a smooth flat surface [web]

Achieving the high ϑs values associated with superhydrophobic materials requires more than chemical repellence alone. It necessitates the combination of chemical repellence with an appropriate surface texture, involving an enhancement of surface roughness, and this is the difference between the hydrophobic and superhydrophobic surface.

The static angle of an ideally smooth reference solid substrate can be expressed via the Young equation, which is retrieved by minimising the net free surface energy of the air(A), liquid (L), solid (S) system:

$$\cos(\vartheta_{s,ref}) = \frac{\gamma_{SA} - \gamma_{SL}}{\gamma_{LA}} \tag{1.3}$$

Where γ represent the surface tension, and the subscripts denote the two phases under consideration conducted experimental studies on the impact of an increase in surface roughness (assuming uniform roughness in all directions) on the static contact angle. This investigation led to the derivation of the following expression:

$$\cos(\vartheta_{s,w}) = r * \cos(\vartheta_{s,ref}) \tag{1.4}$$

The parameter "r" represents the ratio between the actual area of a rough surface and its projection onto a horizontal flat surface, so the water penetrates the corrugation on the surface. For a periodic array of square posts with the dimension shown in figure (1.8), the roughness parameter is given by:

$$r = 1 + 4 * \Phi_S * {}^h\!/_d \qquad \Phi_S = \frac{d^2}{(d+w)^2}$$
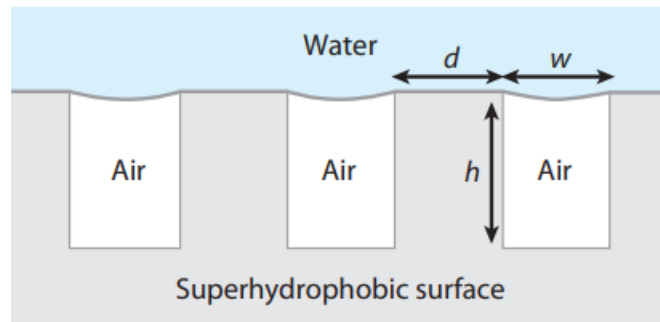

Figure 1-8 schematic representation of a superhydrophobic surface with all the parameter that characterize the surface roughness
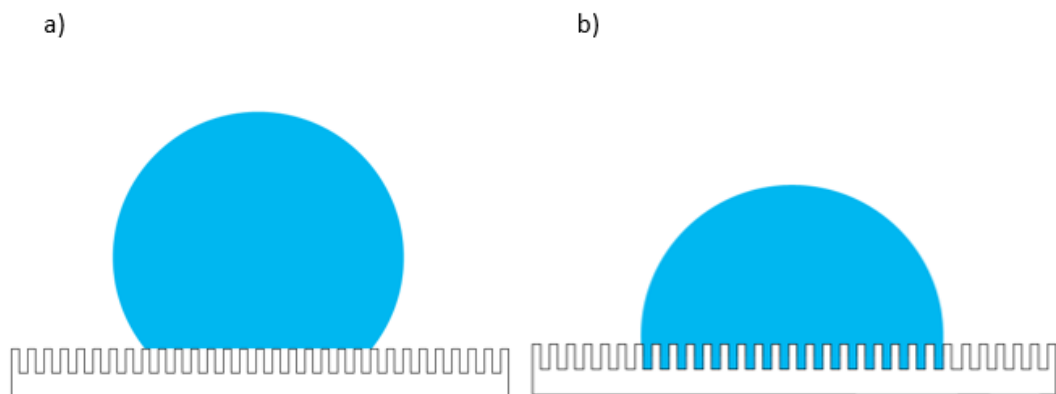
Jonathan P. Rothstein (2009)

Figure 1-9 a) Cassie-Baxter state b) Wenzel state

According to the Wenzel model (figure 1.9b), an increase in "r" is associated with enhanced hydrophobic behaviour, particularly for hydrophobic materials when $\cos(\vartheta_{s,ref}) > 90°$

In contrast, the Cassie and Baxter (1944) model (figure 1.9a) addresses the scenario of a heterogeneous interface, where air is trapped between the liquid and the rough solid. They derived the following expression for this case:

$$\cos(\vartheta_{s,cb}) = r * f_{SL} * \cos(\vartheta_{s,ref}) - 1 + f_{SL}$$
$$= r * \cos(\vartheta_{s,ref}) - f_{LA} * (\cos(\vartheta_{s,cb}) * r + 1) \tag{1.6}$$

or

$$\cos(\vartheta_{s,cb}) = -1 + \Phi_S(1 + \cos(\vartheta_{s,ref})) \tag{1.7}$$

Where f_{SL} represents the solid-liquid fraction and $f_{LA}=1- f_{SL}$ indicates the liquid-air fraction.

An increase of the liquid-air fraction thus results into an increase of the hydrophobicity behaviour, in the case of hydrophobic materials ($\vartheta_{s,ref} > 90°$).

A second indication of the degree of hydrophobicity of a material is the force required to move a drop from the surface. This force is usually provided by the own weight of a drop deposited over the solid surface. The easiest way to implement this test is by tilting the solid plate over which the drop was deposited until the drop start to move. This tilting angle is call roll-off angle ϑ_{ro} (because the drop tends to roll-off rather than sliding).
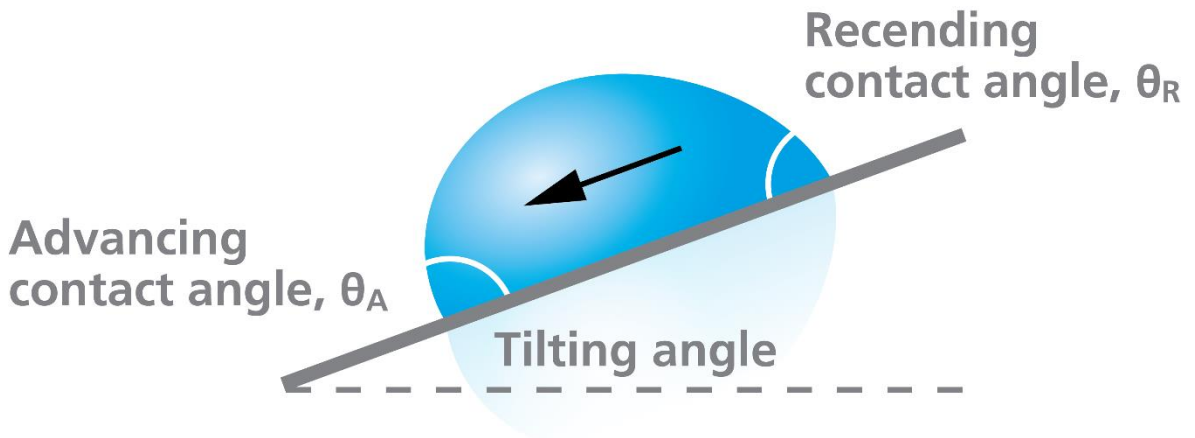

Figure 1-10 Definition of the roll-off angle as the lowest tilt angke that forces the drop to be removed from the solid surface [web]

At ϑ_{ro} the contact angle at the back of the drop ϑ_R in smaller than the one in the front of the drop ϑ_A. The different between the two is called hysteresis angle and measure the energy dissipation energy in the process. In the framework of superhydrophobic surface the roll-off angle and the hysteresis angle have to be close as possible to 0°. There is a practical limit on the post density. For a droplet in the Cassie state, there is a maximum static pressure that can be supported before the air-water interface deflects enough to reach the advancing contact

angle and is driven into the space between the surface roughness. At this point the system reverts to the Wenzel state. Using Young's law Rothstein [3] found:

$$\Delta p_{max} = p_{water} - p_{air} = -\frac{2 * \gamma * \cos(\vartheta_A)}{w} \qquad (1.8)$$

The maximum static pressure that can be supported in the Cassie state decreases with increasing feature spacing.

Let us examine how these principles manifest in the practical application of a superhydrophobic surface: if a surface covered by superhydrophobic coating and characterized by surface roughness is immersed in water, it will create an air layer due to the air trapped within the surface roughness, known as a plastron, it is possible to see the plastron in figure 1.11. This plastron is crucial in applications as it contributes to a reduction in resistance. However, there are still many uncertainties regarding these surfaces, such as the actual drag reduction, deformation, plastron failure, durability etc. Let's analyse what has been understood so far regarding these aspects.

Figure 1-11 Sphere with superhydrophobic coating in a water tank hold by an electromagnetic holder.

1.1.4. Reduction of drag

As we introduced before in the context of drag control, numerous studies have highlighted the advantageous effects of superhydrophobic (SH) surfaces in reducing skin friction at the laboratory scale. Nevertheless, the extrapolation of these findings to broader operating conditions is yet to be demonstrated. In the study of this type of surface, the slip-length model described in the chapter above is a commonly employed boundary condition in numerous numerical simulations and theoretical studies. It is used to represent superhydrophobic (SH) surfaces, ranging from partial slip to perfect slip.

In particular, the first results obtained on superhydrophobic cylinders are the result of You & Moin (2007) and Legendre et al. (2009). You & Moin (2007) analyzed the characteristic features in the near wake, and the sensitivity of the separation angle to external disturbances can be utilized to devise an effective hydrophobic surface scheme where the drag can be reduced. This is done with a numerical analysis, particularly with direct numerical simulations (DNS) and large-eddy simulations (LES) for low Reynolds numbers. The results are in favorable agreement with experimental data and other numerical solutions. Legendre et al. (2009) studied the 2D flow past a circular cylinder also for low Reynolds numbers and investigated the influence of a generic slip boundary condition on the wake dynamics. They found that the slip delays the onset of recirculation and shedding in the wake behind the cylinder, and the drag on the cylinder decreases.

Other experimental results are obtained from Muralidhar et al. (2011). The range of Reynolds numbers analysed is from 0 to 10,000. During their experiments, they used a coated circular cylinder with different micro-size patterns fixed in a test section. When compared to a smooth, no-slip cylinder, the coated surface was found to delay the onset of the vortex, in agreement with Legendre. They also found an increasing length of the recirculation region in the wake of the cylinder. They also demonstrated that the vortex shedding dynamics are very sensitive to changes in feature spacing size and orientation along superhydrophobic surfaces. Other scientists continue this work, analyzing the value of the Reynolds number from 10,000 to 40,000. In particular, Brennan et al. (2014) measured with a laser Doppler anemometer the velocity profile of the water across the wake of a superhydrophobic cylinder. The cylinder in the Cassie-Baxter state showed drag reduction of up to 28% compared to the same in the Wenzel state. The drag reduction shows that the thickness of the plastron and the protrusion height of the features combine to give a drag reduction or drag increase depending on the ratio of the two. In the past few years, Kim & Park (2015) also tried to study that phenomenon. In particular, they analysed a range of Reynolds numbers between 7,000 to 23,000. In this case, the velocity fields were measured using 2D particle image velocimetry (PIV) in a water tunnel. They found a reduction of 40% in the size of the recirculation bubble in the wake because the rough hydrophobic surface was found to enhance the turbulence in the flows above the cylinder and along the separating

shear layer. A drag reduction of less than 10% is estimated. However, this effect is reversed as the Reynolds number increases.

So, in this context, it is possible to collocate my study, which involves Reynolds numbers from 9,000 to 10,500.
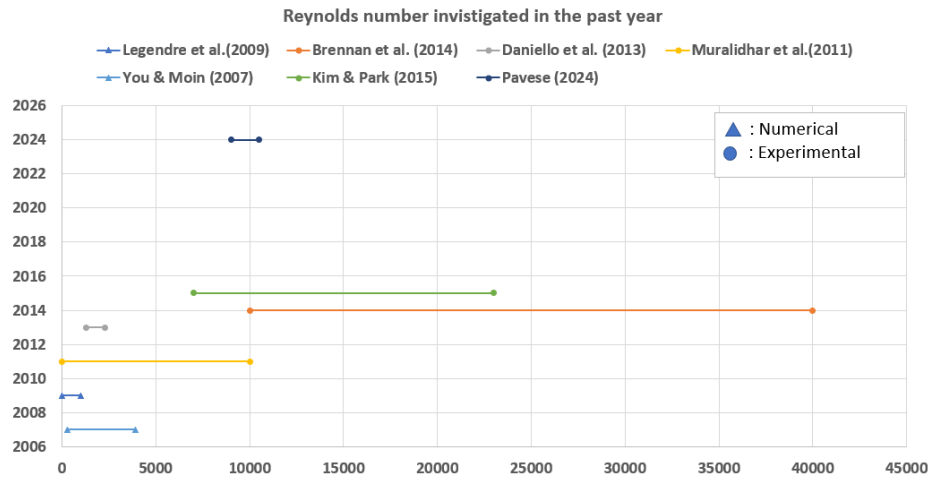

Figure 1-12 previous studies of SH cylinder

In particular, the aim of my study is to measure the reduction of drag and understand which geometric parameter has the biggest influence on it and also the vortex shedding from the trajectory.

Inizio modulo

1.2. Wake of a falling cylinder

In this chapter we investigate the dynamics of the falling cylinder itself without any coating. It could be useful to understand well all the mechanism in the wake generation.

The objective of this chapter is to elucidate the vortex dynamics phenomena that occur over a wide range of Reynolds numbers (Williamson (1996)) for a normal cylinder. This could help us in the comparison between the vortex dynamics for a normal cylinder and for an SH cylinder.

A key element for such a discussion involves the plots of the pressure coefficient (C_p) as a function of Reynolds number and it is possible to link this discussion with the variation of the C_d (in figure 1.13 it is possible to see the pressure coefficient over a cylinder). In contrast to some other parameters of the flow, the base pressure responds sensitively to changes in flow instabilities and phenomena throughout the Reynolds number range.

The Reynolds number for a cylinder is defined as:
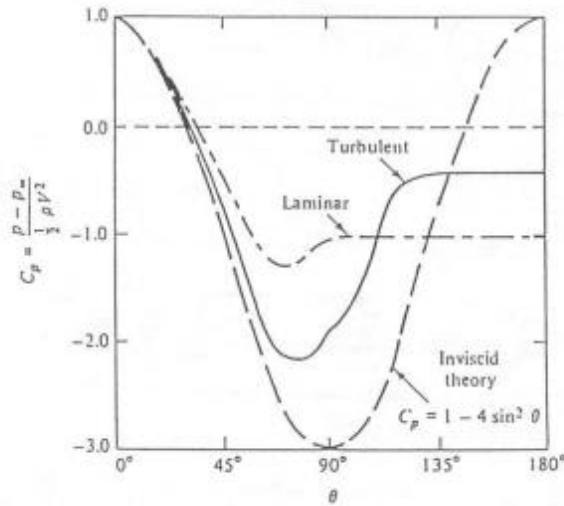
$$Re = \frac{\rho v D}{\mu}$$

Figure 1-13 Pressure coefficients over a cylinder, for laminar, turbulent and inviscid flow condition

[Bruschi et al. (2003)]

Before this discussion it is important to understand the link between these two parameters C_p and C_d.

The total pressure drag on the cylinder is calculated by integrating the differential pressure components over the surface of the cylinder. Each differential pressure component (p) acts in the opposite direction of the surface normal and must be projected along the direction of travel to obtain its contribution to total pressure drag.

$$F_{D,p} = \int \int p(\theta) * \cos(\theta) \, da \qquad (1.10)$$

θ is the angle between the drag direction and the surface normal.

These values are a function of position and must be integrated over the surface area to obtain the pressure drag force, $F_{D,p}$. By making the approximation that $F_D \approx F_{D,p}$, the coefficient drag can be write as:

$$C_D \approx C_{D,p} = \frac{\int \int C_p * \cos(\theta) \, da}{A} \qquad (1.11)$$

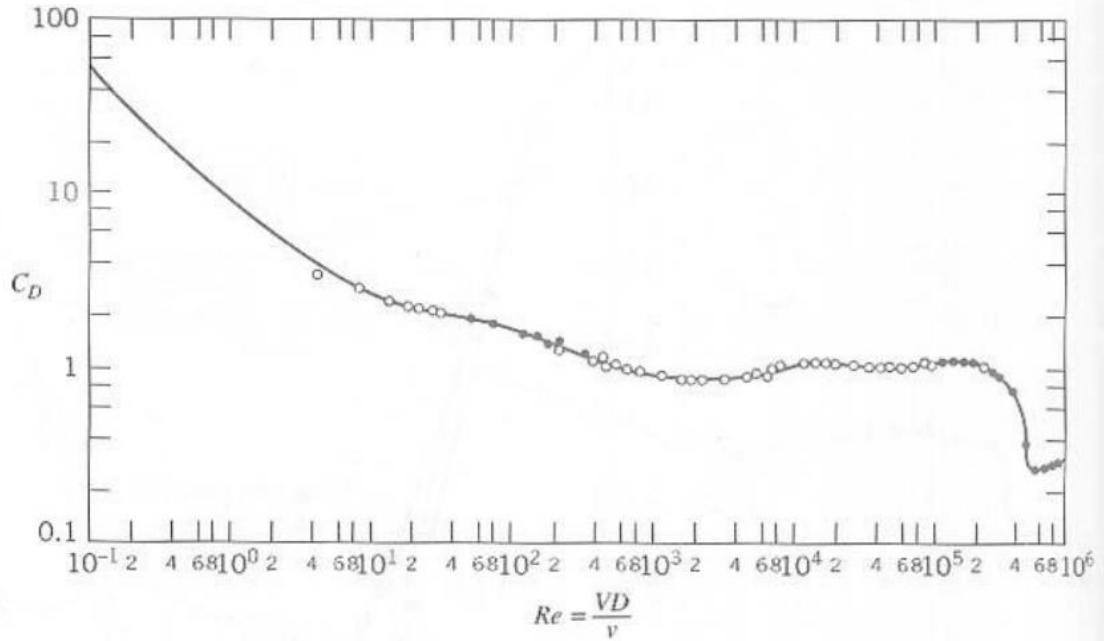A is the cross-sectional area because the cylinder may be considered a blunt object

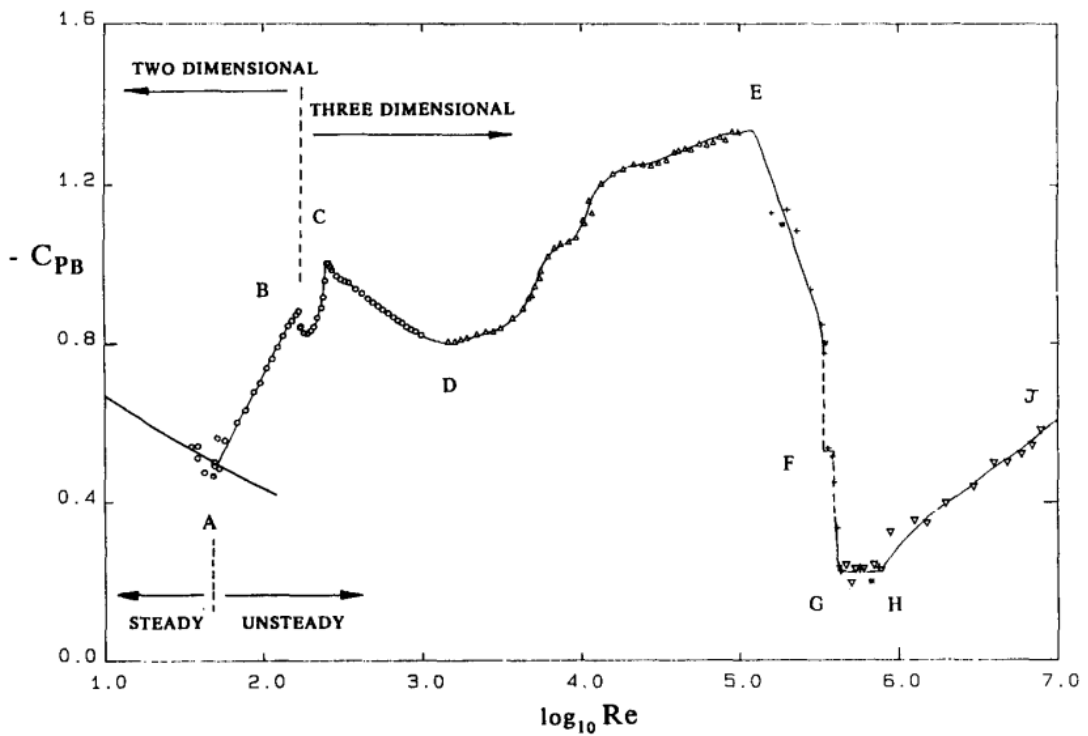*Figure 1-14 plot of the drag coefficient over a large Reynolds number*

*Figure 1-15 Plot of base suction coefficients (-Cpb) over a large range of Reynolds numbers. Data: 0, Williamson & Roshko (1990); A, Norberg (1987); +, Bearman (1969); *, Flaschbart (1932); v, Shih et al (1992). Curve for steady flow regime (Re < 49) is from steady computations of Henderson (1995). [Williamson (1996)]*

As we can see the two figures above (1.13 and 1.14) have the same tendency.

In the section below, the analysis focuses on the different regions in Figure 1.14. It is crucial to comprehend the dynamics of the wake and determine the critical Reynolds number before delving into the study of superhydrophobic surfaces.

At Reynolds number below approximately 49, the wake consists of a steady recirculation region of two symmetrically placed vortices on each side of the wake, and their length increases with the Reynolds number.
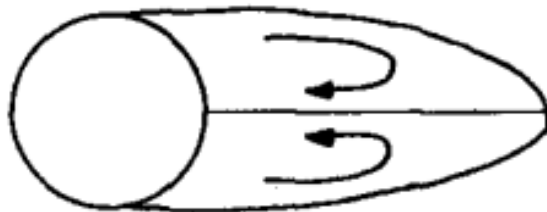
*Figure 1-16 The vortical wake from a bluff body can be steady, forming
a pair of recirculation regions behind the body*

It should be noted that with an increase of the length of the steady wake bubble, caused by viscous stresses, there is a corresponding decrease in the base suction. This regime is called laminar steady regime.

In the laminar vortex shedding regime (Re = 49 to 140-194), the variation of base suction with Re shows a sharp deviation in trend from the steady wake regime above. The recirculation region develops instabilities, whose strength and amplification grow with Re. This effect may be measured by a monotonic increase in the amplitude of maximum wake velocity fluctuations with Re and a gradual movement of the instability maximum (or formation length) upstream toward the cylinder (Williamson 1995).

As the wake instability becomes amplified, the Reynolds stresses in the near-wake region increase, the formation length decreases, and there is a consistent increase in the base suction The wake oscillations are purely periodic over this complete regime. This transition regime

(Re - 190 to 260) is associated with two discontinuous changes in the wake formation as Re is increased. The discontinuities may be manifested by the variation in Strouhal number (Williamson 1988).
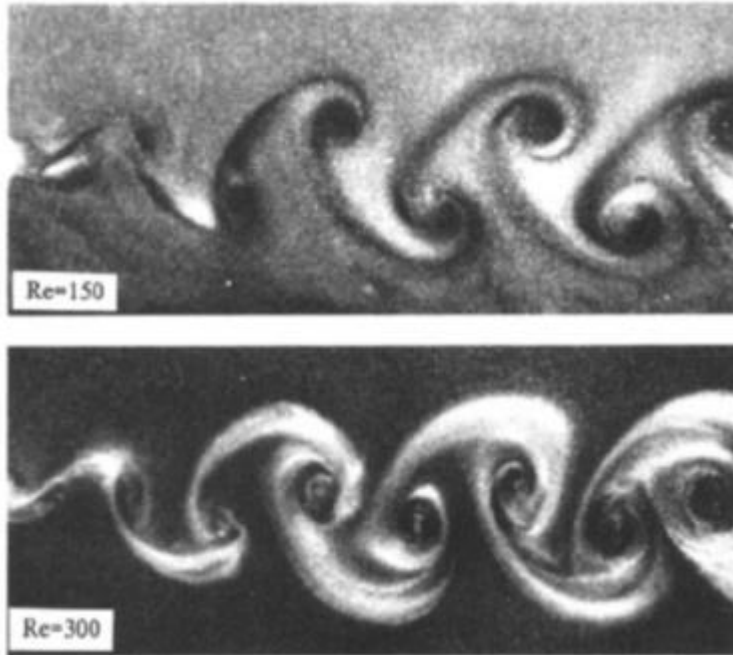
At the first discontinuity, occurring near Re = 180-194 (depending on experimental conditions), the inception of vortex loops and the formation of streamwise vortex pairs were observed due to the deformation of primary vortices as they are shed, at a wavelength of around 3-4 diameters. This discontinuity is labelled as a "hard" transition by Zhang et al (1995).

Figure 1-17 Visualization of laminar and turbulent vortex streets. These photographs show the development of Karman vortex streets over a wide range of Re. Streamwise vorticity, in the braid between Karman vortices, is indicated by the white regions The visualizations are from Williamson (1995a).

The mode of Re from 230 e 250 comprises finer-scale streamwise vortices, with a spanwise length scale of around one diameter. The large intermittent low-frequency wake velocity fluctuations, have been shown to be due to the presence of large-scale spot-like "vortex dislocations" in this transition regime (Williamson 1992). These are caused by local shedding-phase dislocations along the span. The base suction and Strouhal frequency continue to increase in this regime.

The peak in base suction at Re = 260, is associated with a peak in Reynolds stresses in the near wake and a particularly ordered 3-D streamwise vortex structure in the near wake (Williamson 1995). At this point, the primary wake instability behaves remarkably like the laminar shedding mode, with the exception of the presence of the fine-scale streamwise vortex structure (Williamson 1995, Prasad & Williamson 1995)

As Re is then increased towards point D in the plot, the fine-scale three dimensionality becomes increasingly disordered, and this appears to cause a reduction in the two-dimensional Reynolds stresses, a consistent reduction in base suction, and an increasing length of the formation region (Una1 & Rockwell 1988, Williamson 1995a)

In the shear layer transition regime (Re = 1,000 to 200,000), the base suction increases, the 2-D Reynolds stress level increases, the Strouhal number gradually decreases, and the formation length of the mean recirculation region decreases (Schiller & Linke 1933), all of which are again consistent variations. Roshko (1993) associated this regime with an increase

in base suction and drag, while the turbulent transition point in the separating shear layers moves upstream, as Re increases.

The increase in formation length that we observed in the previous regime C-D, and the decrease in formation length in the present regime, are very well demonstrated by the visualizations of Una1 & Rockwell (1988) and the PIV (Particle-Image-Velocimetry) experiments of Lin et al (1995a). Three dimensional structures on the scale of the shear layer vortices are expected to develop in this regime.
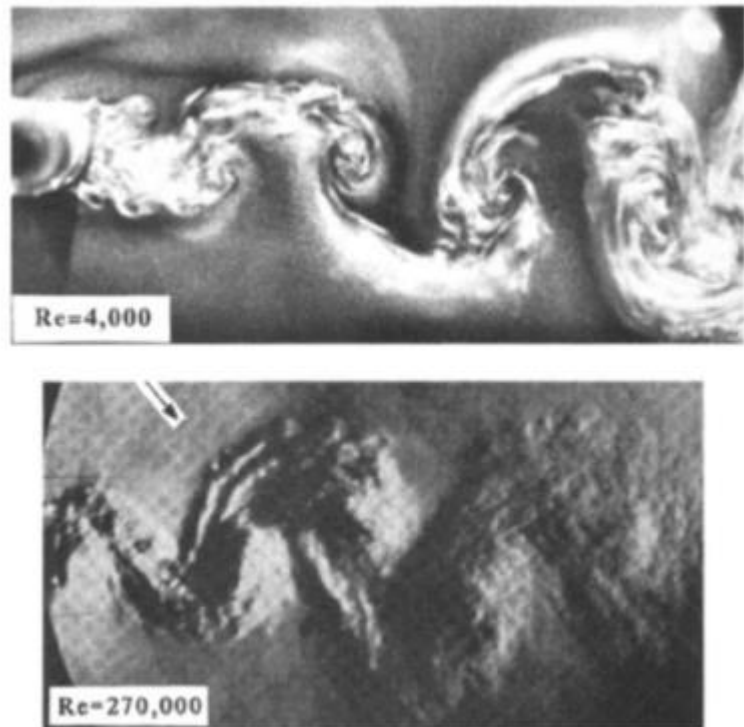

Figure 1-18 Visualization of laminar and turbulent vortex streets. These photographs show the development of Karman vortex streets over a wide range of Re. Streamwise vorticity, in the braid between Karman vortices, is indicated by the white regions The aluminum flake visualization is from Williamson (1995a). The Schlieren photograph at Re = 270,000 is from Thomann (1959).

In the region E-G (critical regime) the base suction and the drag decrease drastically. This is associated with a separation-reattachment bubble, causing the revitalized boundary layer to separate much further downstream and with a much-reduced width of downstream wake than for the laminar case. The most significant phenomena occur in F, where there is the separation-reattachment bubble on only one side of the body

In the supercritical regime (region G-H), the flow is symmetric with two separation-reattachment bubbles, one on each side of the body. Fluctuations are detected in the wake at large Strouhal numbers of around 0.4 (Bearman 1969). According to Roshko (1993), the considerably higher Reynolds stresses of the boundary layer following the separation bubble allow the boundary layer to survive a greater adverse pressure gradient than in the post-critical regime, where transition finally occurs before separation.

The effect of an increase in Re up to this particular regime (H-J) is to move the turbulent transition point further upstream, until at high enough Re, the boundary layer on the surface of the cylinder itself becomes turbulent.

In 1961, Roshko was able to demonstrate the surprising result that periodic vortex shedding is strongly evident even in this flow regime.

Once the vortex analysis is done, it is important to analysed the effect of this vortex on the trajectory of the cylinder in particular, reference was made to the experiment conducted by Horowitz & Williamson (2010)

The experimental campaign by Horowitz & Williamson involved an experiment very similar to the one conducted in the PRISME laboratory, albeit with a completely different purpose. This experiment was useful to get an idea of the results that would have been approximately obtained without the super-hydrophobic surface.

They discover that trajectory of the cylinder change based on the value of m^*:

$$m^* = \frac{m}{\rho * \pi * \frac{D^2}{4} * L}$$

(1.12)

It was funded that if the mass ratio is greater than a critical value, $m^*_{crit} = 0.545$, the body falls or rises with a rectilinear trajectory. As the mass ratio is reduced below $m^*_{crit} = 0.545$, the cylinder suddenly begins to vibrate vigorously and periodically.
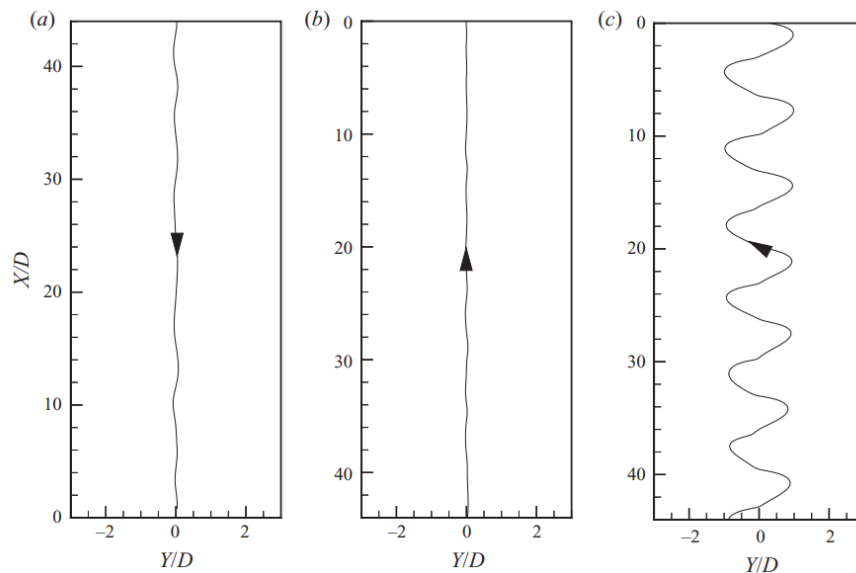

Figure 1-19 Trajectories of freely rising and falling cylinders. (a) m ∗ = 1.99, Re = 9000; falling cylinders descend rectilinearly. (b) m ∗ = 0.78, Re = 5000; some rising cylinders can also move with rectilinear trajectories. (c) m ∗ = 0.45, Re = 3800; a very light rising cylinder exhibits vigorous vibration (A ∗ Y = 1.0). It should be noted that the Y -axis of these trajectories is significantly expanded relative to the X-axis, so that the non-periodic transient motions in (a) and (b) are, in reality, extremely small. The trajectories in (b) and (c) appeared previously in Horowitz & Williamson (2006) [Horowiyz and Williamson (2010)]
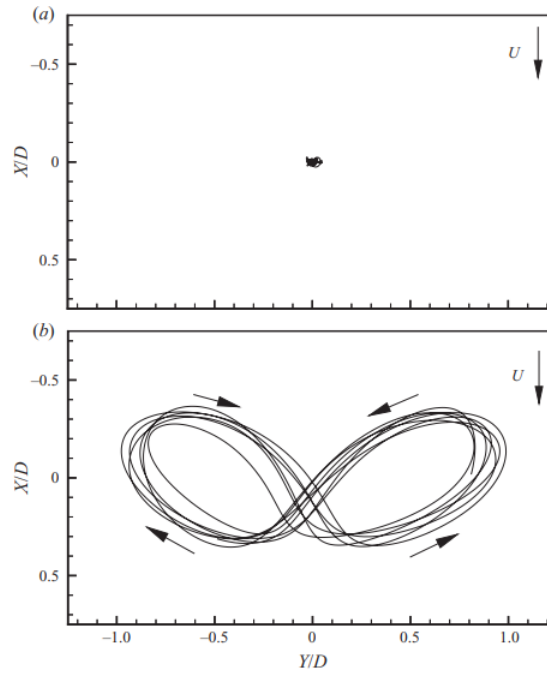
Figure 1-20 Lissajous figures for freely rising and falling cylinders. (a) m ∗ = 0.78, Re = 5000; cylinders with rectilinear trajectories show only small non-periodic motion in both transverse and streamwise directions. (b) m ∗ = 0.45, Re = 3800; rising cylinders vibrating in the transverse direction also exhibit significant streamwise oscillations (A ∗ X ≈ 0.3), producing a figure-of-eight shape [Horowiyz and Williamson (2010)]

In studies of rising and falling bodies, it is common to characterize the system using the mass ratio, m^*, and the Galileo number:

$$Ga = \frac{\sqrt{|m^* - 1|gD^3}}{\nu} \qquad (1.13)$$

(These quantities depend only on known parameters of the fluid and the body)

For both the cylinder they used, a jump from rectilinear motion (shown by open symbols) to periodic vibration (solid symbols) occurs when the mass ratio falls below m∗ crit = 0.545 ± 0.01. This value of the critical mass appears to be valid in the range of Galileo numbers Ga ≈ 5000–9000.

This study holds significance in the selection of the cylinder, aiming to prevent vibrations that can amplify the intricacies of post-processing, specifically in the evaluation of displacement.

2. Experimental set up

The first step in setting up the experiment was to replicate the setup conducted by Marco Castagna (2019) concerning the falling sphere in the PRISME laboratory. Initially, the experiments were conducted without the coating, solely to study the dynamics of the falling object. Subsequently, the experiments were repeated with the superhydrophobic surface. The primary goal of these experimental campaigns was to alter the shape of the object to better observe the air layer generated by the superhydrophobic surface and its deformation. The initial attempt involved using a cylinder.

2.1.   Choice of the geometry

The initial experiment was conducted using a sphere to simulate the experiment of Castana, and subsequent considerations led to the decision of altering the geometry for enhanced observations. A cylinder emerged as a favorable alternative, proving beneficial for scrutinizing plastron deformation more effectively than the sphere that could be useful for the future study.

The inaugural experiments involved a steel cylinder. It was used two different steel smooth cylinders without any coating. The specifics of the first cylinders are outlined in Table 2.1.

	Cylinder 1	Cylinder 2
D	10mm	16mm
L	27mm	67mm
AR=L/D	2.7	4.18

Tab. 2.1. Dimensions of the first cylinder studied

An important parameter is the aspect ratio, define as:

$$AR = \frac{L}{D_{ext}}$$

(2.1)

in this case due to the dimension of the tank, it is difficult to reach a high value, that probably help the stabilization during the falling.

Moreover, the initial experiments with the cylinders in Tab. 2.1 revealed a tilting movement that posed challenges during the post-processing phase. This tilting motion resulted in inaccuracies in the code outputs. And moreover, this complicates the analysis in the mirror view, in fact this compromised visibility of the lateral part of the cylinder because we can't
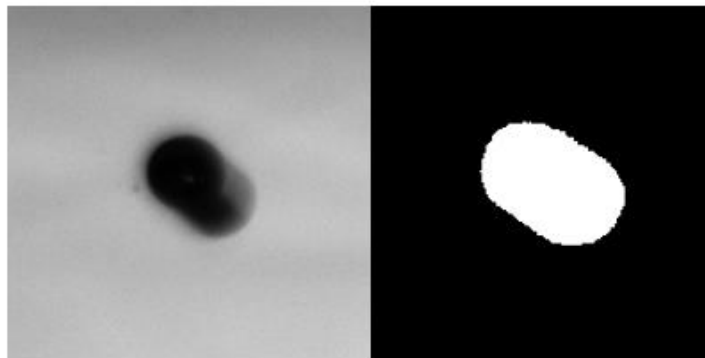
Figure 2-1 Images from the experiment of the mirror view on the left it is possible to see the photo on the right the binarized image
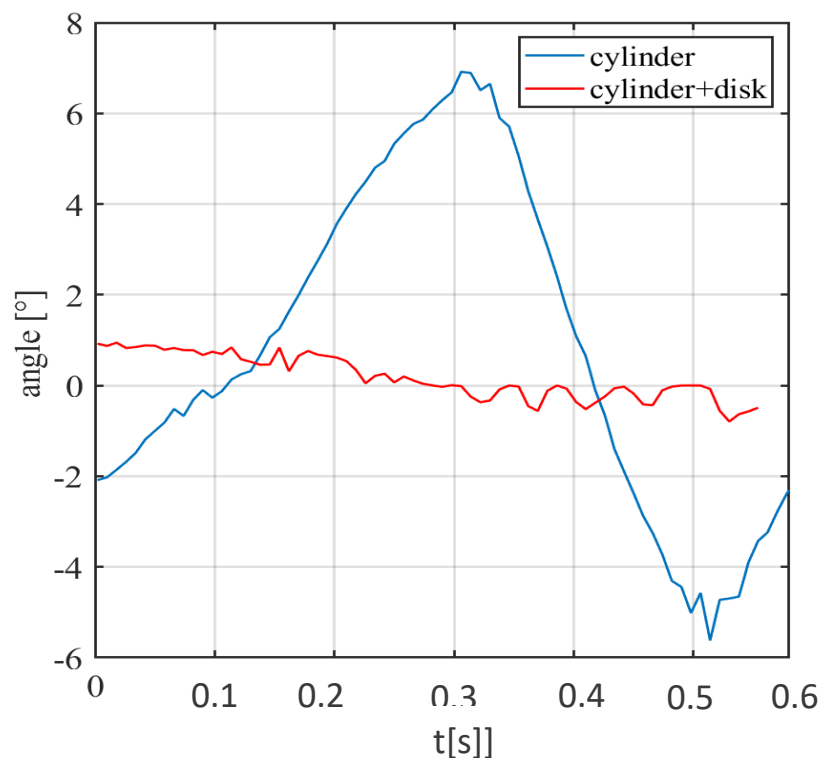

Figure 2-2 Variation of the angle of the cylinder with the horizontal line in function of the time for a cylinder of D=10mm and L=27mm for the blue line and the same dimensions but with two of 50mm for the red line

distinguish the lateral side with the ended part of the cylinder, impacting the accuracy of the movements (mirror view shown in figure 2.1.).

Attempts were made to assess the variation in the angle of the cylinder during its descent, as we can see in Figure 2.2 the blue line is characterized by a huge variation of the angle during the falling. To address this issue, the introduction of disks at both sides of the cylinder was contemplated. The disks we used are transparent, so it possible to see though them. This modification effectively resolved the problem. In fact, as we can see in figure 2.2 for the cylinder with the disk (red line) the variation of the angle is visibly reduced.

For the initial steel cylinder, a 50mm-diameter disk was introduced, whereas a 70mm-diameter disk was implemented for the second cylinder. I also try other sizes of disks but in the end the current size was found to be the most suitable. After all the experiments with these cylinders and developing a post-processing code that works effectively, we transitioned to the study of superhydrophobic surfaces.

2.2. Superhydrophobic cylinder: characterization of dimension and surface

For the design of the superhydrophobic surface cylinder, a new configuration was necessary. In this instance, the external part of the cylinders was fabricated using a 3D printer with specific surface roughness. The selection of the cylinder parameters was based on achieving the instabilities of the plastron in the bigger tank, which is the larger of the two. Simultaneously, the goal was to attain the final velocity. A theoretical calculation was employed, analysing variations in parameters such as density, diameter, and length of the cylinder.

In this scenario, as previously mentioned, the external section of the cylinder is composed of plastic. The internal component serves the purpose of augmenting the cylinder's weight, and in my specific case, a steel rod was employed (figure 2.3). Prior to selecting this configuration, various materials with distinct densities were deliberated upon. In fact, in the future, another study could involve changing the density of the internal rod, thereby altering the velocity and observe what happens to the drag coefficient.
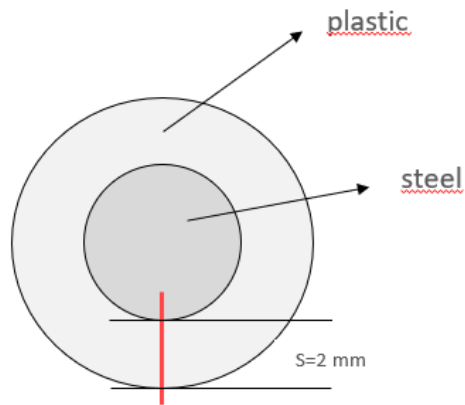
Figure 2-3 Simplified drawing of the side view of the cylinder

For the evaluation of the un-known parameter necessary for the evaluation of the C_d it was used the formula:

$$\sum F = m * a \qquad (2.2)$$

The force acting on the cylinder are: the weight, the drag and the Archimedes force as shown in the figure below (2.4):
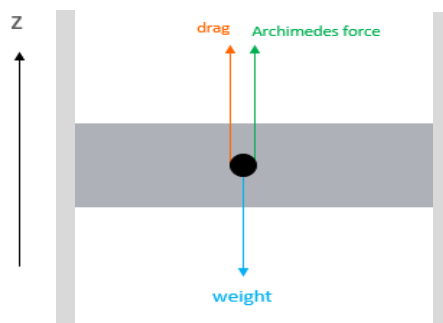

Figure 2-4 Force acting on the cylinder during the falling

It is possible to rewrite the same equation:

$$-m_s * g + \frac{1}{2} * \rho_L * D * L * v^2 * c_D + vol * \rho_L * g = m_S * a + \frac{1}{2} * m_L * a \qquad (2.3)$$

From this equation and using figure of C_d-Re (1.14) it was possible to evaluate a prediction of the parameters. In particular the important one is the height of the tank at which I reach the final velocity, the Reynolds number and the value of the drag coefficient.
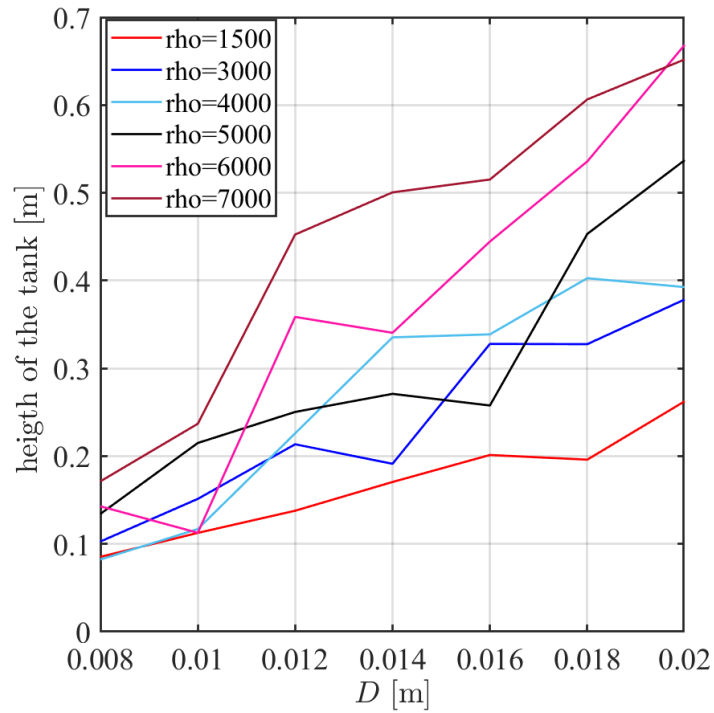

Figure 2-5 Variation of the height of the tak when the cylinder reaches the final velocity depending on the variation of the diameter and the density of the mass
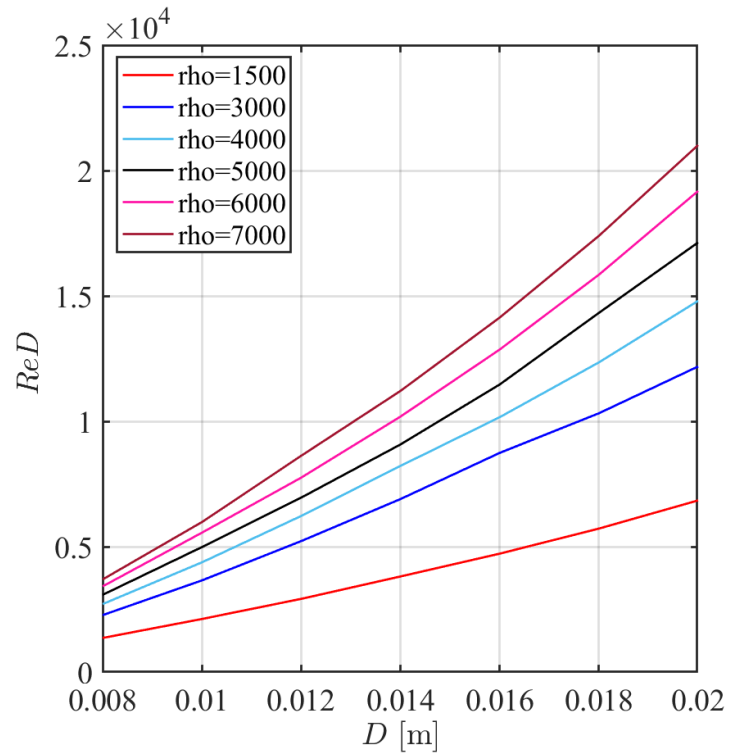
Figure 2-6 Variation of the Reynolds number over the diameter with the variation of the density
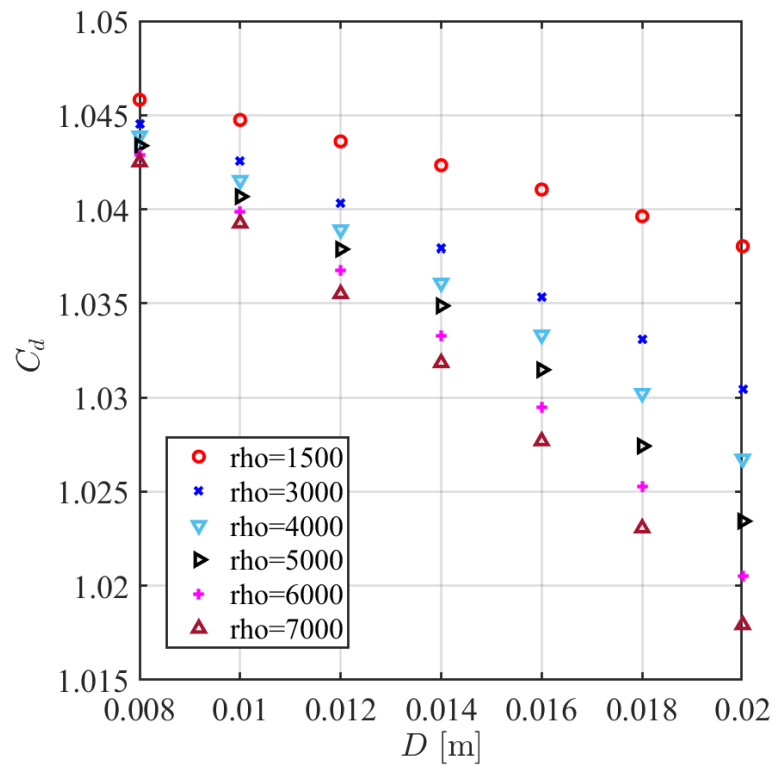

Figure 2-7 variation of the drag coefficient over the Reynolds number with the variation of the density (it is not considered the drag coefficient of the disk)

In the first figure (2.5) it is possible to see that if we increase the diameter and the density (→ increase the mass value) the high at which the final velocity is reach increase. In figure 2.6 illustrates that a higher mass corresponds to a higher Reynolds number because it corresponds to higher velocity. The figure does not depict the length of the cylinders as it is independent of the final velocity. In the last figure it was represented the drag coefficient, this latter decreases both with increasing diameter and with increasing density of the internal part.
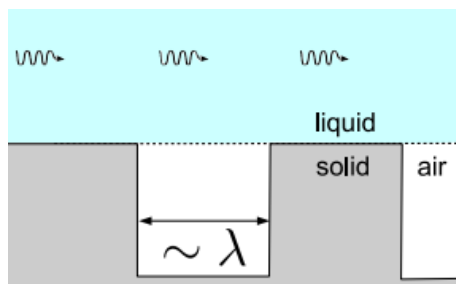
Based on these graphs, the final decision was made to choose an external diameter D_{ext}=15mm and an internal diameter D_{int}=9mm (diameter of the steel rod), with a thickness of the plastic of about 2mm. The length of the cylinder is imposed at 13.7mm, this doesn't have any influence in the final velocity but it was chosen to have a high aspect ratio. In fact, as we mentioned before, it could help in stabilizing the cylinder. But at the same time it has not to be too much high because overwise we increase the risk of the hitting of the wall during the falling in this particular case the aspect ratio is about 10 which is close to the one used by Horowitz et al. (2009) in its experiment.

For the roughness, the calculation was based on the Weber number. There are two different definitions of this number as describe by Castagna (2019), in particular the Weber number based on the diameter (which is the ratio between the separation-induced suction and the capillarity pressure described before):

$$We_D = \frac{\rho_l u_D^2 d}{\gamma} \tag{2.4}$$

And the weber number based on the roughness:

$$We_\lambda = \frac{\rho_l u_0^2 \lambda}{\gamma} \tag{2.5}$$

Figure 2-8 Representation of the geometry of the superhydrophobic surface [Marco Castagna (2022)]

In the current case the useful one is the second one We_λ, in particular we know that $We_{\lambda,cr} = 0.3$ and so we want a higher value. Imposing a value higher it was possible to find the dimension of the of the roughness element λ. λ is the space between two different pillar, shown in the figure 2.8

After the evaluation of the roughness element, it was possible to draw the three cylinders in a CAD program. In figure 2.9. it is possible to see one of them.
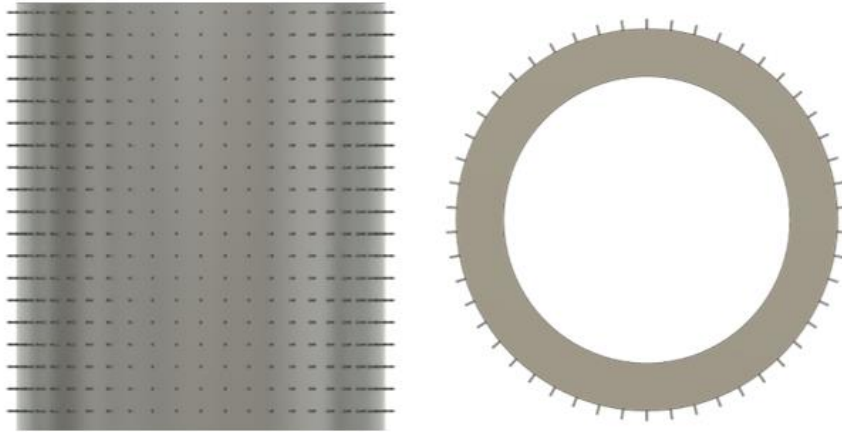

Figure 2-9 CAD image of one the cylinders, in particular the cylinder 4

At this point, it was possible to proceed with the printing. For practical reasons, it was not possible to print a single cylinder of 13.7 cm, but it was necessary to print two separate ones. These will then be held together by the steel rod and compressed by the two disks on the sides. In figure2.12 it is possible to see the union of the two cylinders and in details the surface roughness
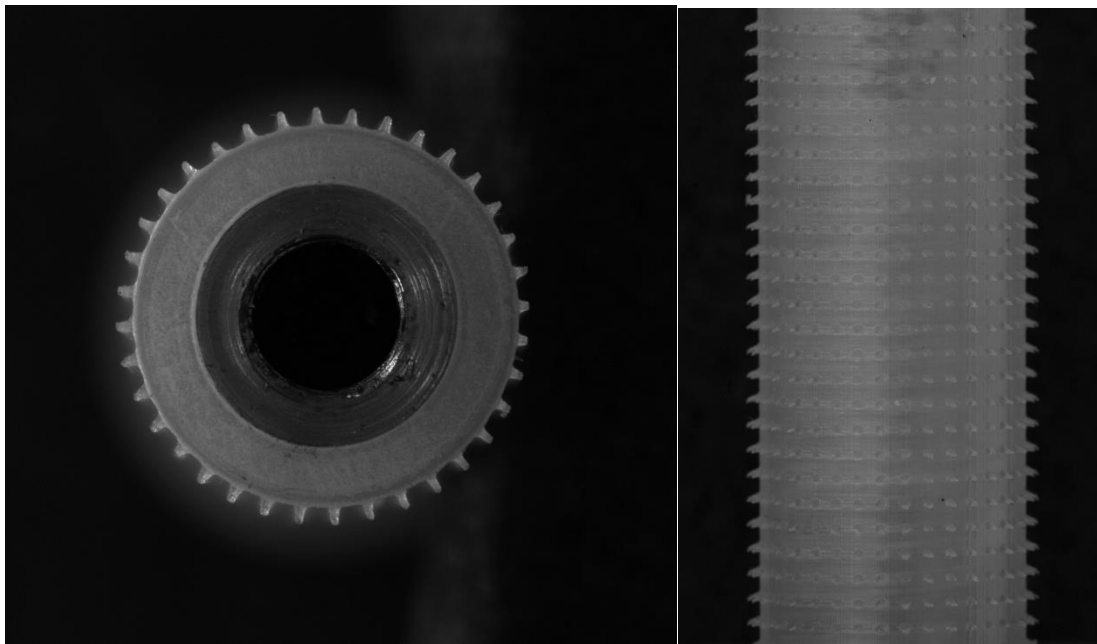

Figure 2-10 Photo of the roughness of a cylinder

As we told before the experiments are done with three different cylinders, so in the tab 2.1 we introduce the caracterizationof these 3, but also an other cylinder used as reference with a smooth surface. (in figure 2.11 it is possible to see the different parameters)
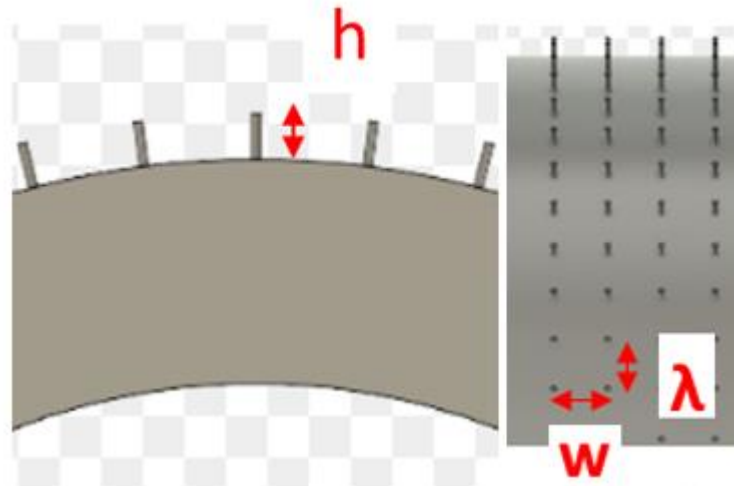

Figure 2-11 Parameter of the roughness

	Cylinder 1	Cylinder 2	Cylinder 3	Cylinder 4	Cylinder5	Cylinder6	Cylinder7
D [mm]	15						
L [mm]	137						
Aspect Ratio (L/D)	9.13						
H(mm)	0	0.69		0.49		0.46	
λ=w [mm]	0	0.39		0.48		0.83	
λ/h	0	0.57		0.98		1.80	
Coating	no	yes	no	yes	no	yes	no

Tab. 2.2. Characterization of the cylinder used during the experimental part

These parameters were assessed not from the CAD drawing but through the photo in Figure2.10. Indeed, thanks to the graduated scale (figure 2.12), calibration was possible, and the various parameters were measured using the ImageJ software.
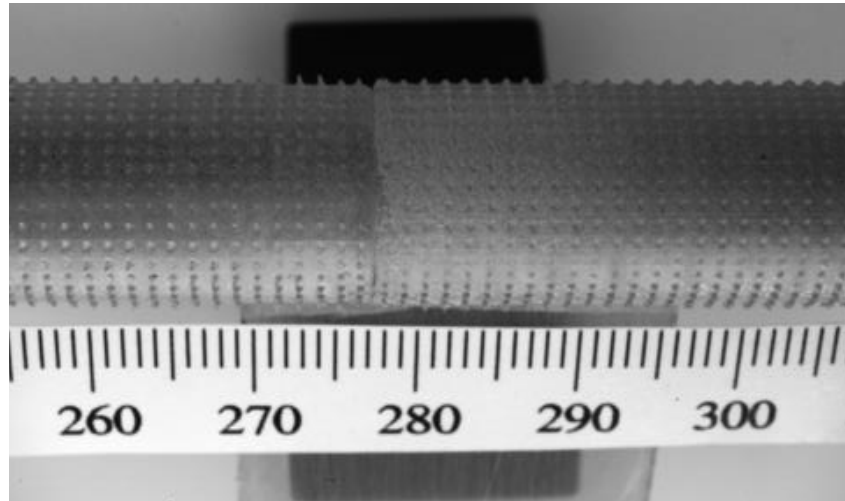
Figure 2-12 Calibration image

Now the cylinders are ready for the coating.

2.3.   Manufacture of the cylinder: Spray coating method

The properties of the superhydrophobic surface are achieved through the application of a commercially available product: Ultra-Ever Dry. This product comprises two layers, namely the bottom and the top layers. It is formulated as a polymer dissolved in solvents in the first case the propanol and in the other the xylene. Upon spraying, the solvents evaporate upon exposure to air, leaving only the polymer on the surface. Achieving a uniform coating on the cylinder proves to be challenging. The process involves utilizing a support and rotating it to ensure that the entire surface is evenly painted.

The implemented manufacturing procedure was designed as follow:

1) Al the surface is clean both the one of the cylinders and al the object used during the procedure.
2) The bottom coating was uniformly sprayed over the surface (it takes one hours for the drying)
3) The topper coating is spray to obtain the SH surface, and in this case one wall night dry time was imposed.

This type of coating is very delicate and it is not possible to touch by hand.

Ultimately, to estimate the cost of the product necessary for the creation of the coating, at the time of drafting this text, it averages around 250 euros/l for both the bottom and top coatings. With this quantity, an approximate coverage of 6m^2 can be achieved

After this procedure the cylinder are ready for the experiment.

2.4. Experimental rig for the sphere and cylinder drops

The first experiment took place in a transparent tank with a square cross-section, measuring 100 mm in width and 650 mm in height. The choice of a square cross-section was preferred over cylindrical walls to avoid optical distortion. The tank was filled with pure water, and the liquid's temperature was monitored using a thermocouple. Due to the use of pure water, a moving system to measure the gradient of temperature like the one used by Castagna was not necessary, as water viscosity remains relatively constant with small temperature variations. The temperature was maintained at around 20°C by the surrounding environment.

An electromagnetic holder was utilized to submerge the ferromagnetic sphere beneath the liquid surface. The electromagnetic holder, consisting of a coil
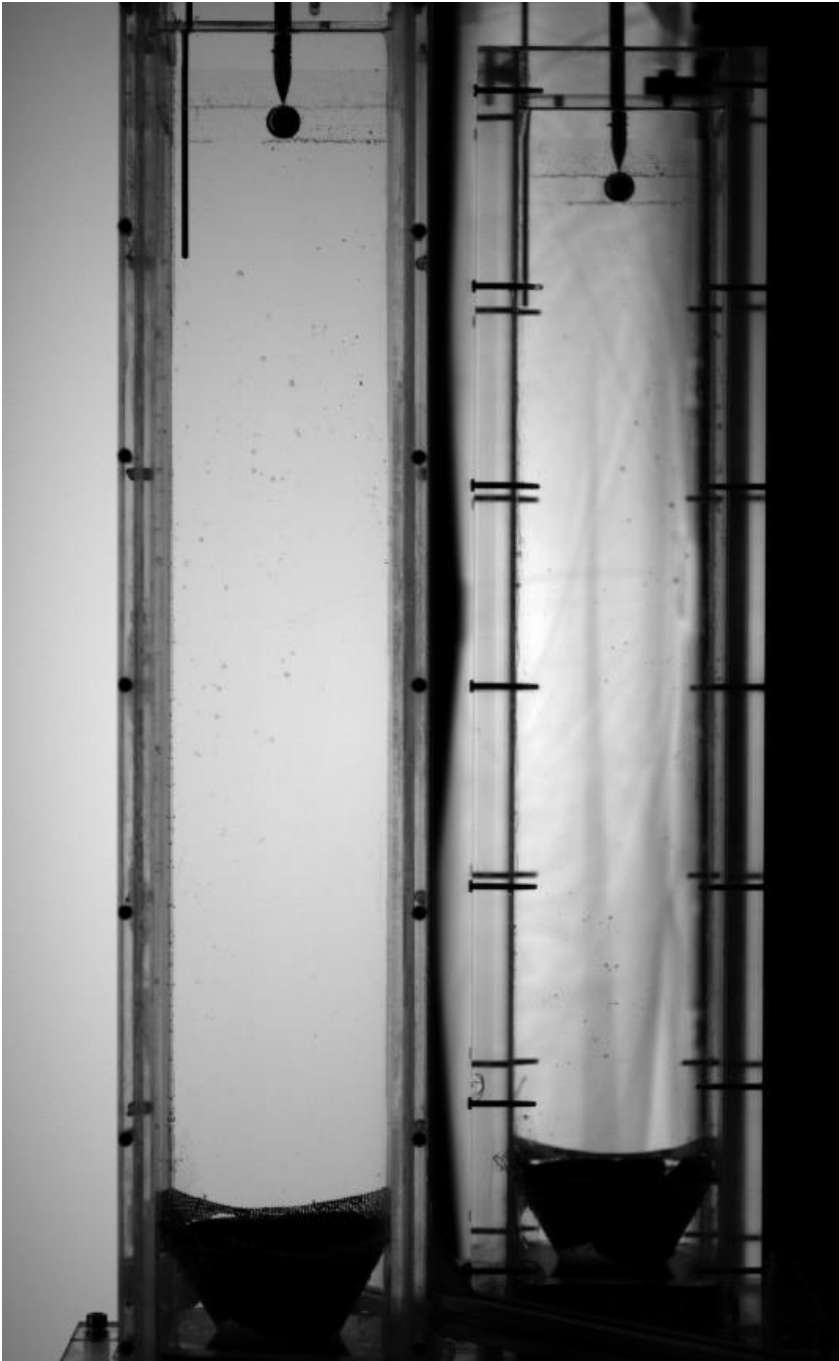
Figure 2-13 Set up for the sphere seen by the camera

and a rod with a sharp tip to limit contact with the sphere surface and prevent damage to the superhydrophobic coating, required the sphere to be ferromagnetic for proper functioning.

Spheres with different diameters made of steel were employed for the experiment, allowing for the manipulation of different Reynolds numbers based on their weight and resulting constant velocities.

Experimental data were captured using a high-speed camera capable of recording the entire sphere drop. The camera used an auto-trigger functionality to detect the initial movement of the sphere within a user-defined control region of the image. Placed in front of one side of the tank wall, the camera provided a view of the (X, Z) plane. To observe both the (X, Z) plane and the (Y, Z) plane simultaneously, a mirror was positioned at a 45° angle to the tank side wall, crucial for a reliable cross-correlation algorithm and the recreation of the 3D trajectory

Black lights placed behind the front and side recording planes were essential for providing sufficient contrast.
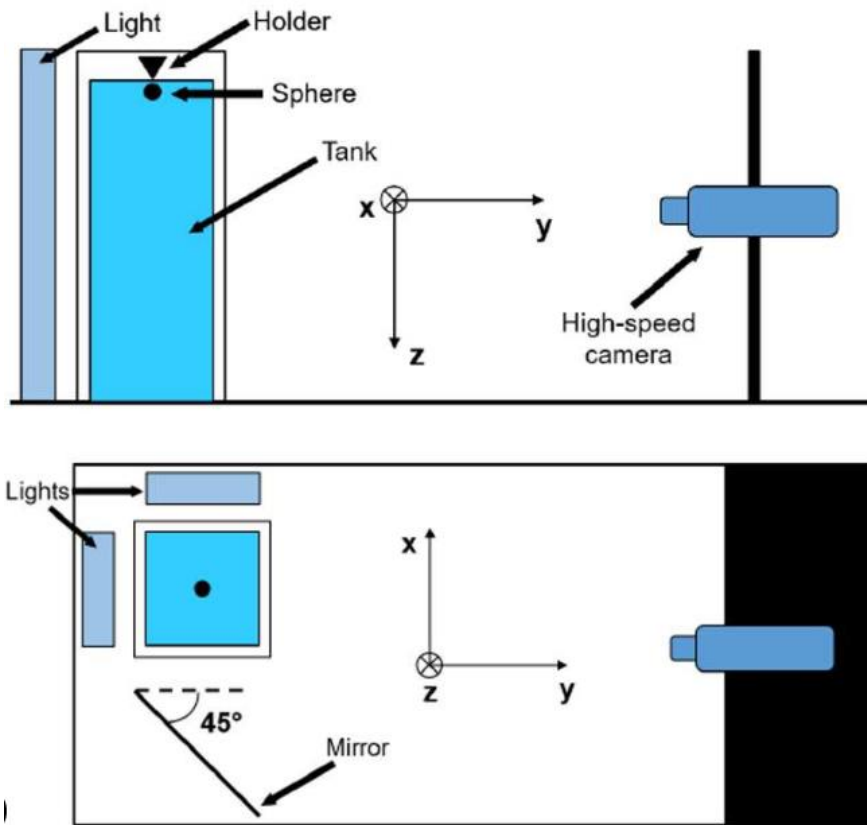

Figure 2-14 Schematic of the falling sphere experimental rig, side and top view
(Marco Castagna (2019))

The test commenced by cutting off the power to the electromagnetic holder, allowing the sphere to drop, and activating the camera. Recovering the sphere from the end of the tank was facilitated by a double valve in the lowest part of the tank, minimizing water loss. After the first experiment with the sphere, we use almost the same set-up also for the cylinder.
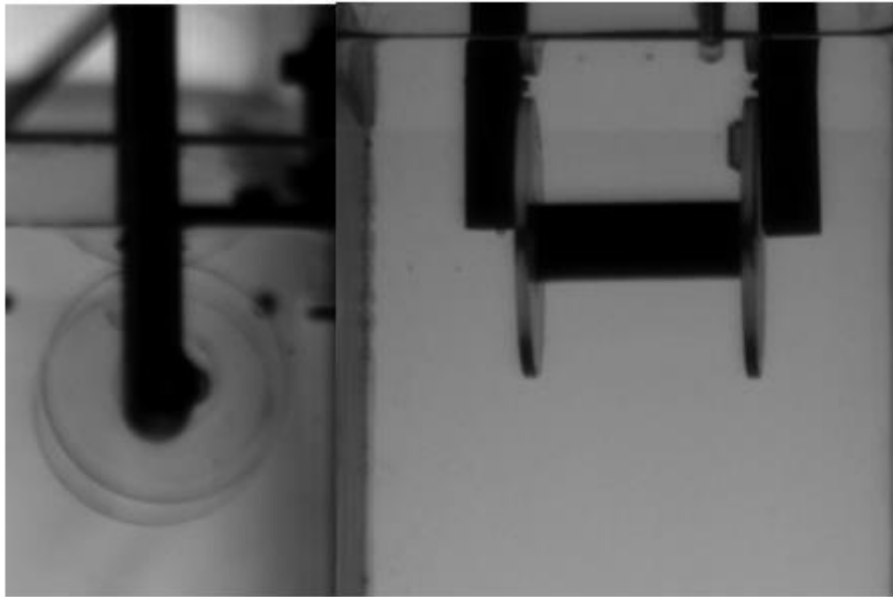
Figure 2-15 Support for the cylinder (front e mirror view)

In this case, the setup differs in the release system and the sphere recovery method. The release system employs a mechanical setup with one fixed arm and the other moved by an electric motor with a sensitivity of $10^{-6}m$. This precise holder allows for the use of different materials beyond just steel, as was the case with the sphere. This difference will be crucial during the use of superhydrophobic surfaces, where a plastic material is employed to generate the required surface roughness. In this way, it is also possible to avoid damaging the hydrophobic surface through contact with other surfaces, something that, on the other hand, used to happen in the case of the sphere. The drop initiates when the second arm moves.

This solution was not the optimal one because it required the cylinder to be perfectly aligned; otherwise, it would start to rotate, posing potential issues due to contact with the rear wall.

Another difference is in the method of cylinder recovery after falling because the double valve cannot be used anymore. Therefore, we no longer need the cone positioned at the end of the tank, which was intended to channel the sphere into the first valve. The easiest solution was to use in this case is a magnet to pull it up for the steel cylinder.

For the second phase of the experiments, the same setup was utilized, but with a larger tank measuring 20cm x 20cm x 1m. This allowed for the use of larger cylinders, particularly

those with a higher aspect ratio. In this instance, a pump was installed to facilitate container filling.

2.5. Camera settings

The main challenge with the camera was finding a balance between having a sufficiently large field of view to include both the front and side planes and maintaining high spatial and temporal resolution. After analysing this issue, it was determined that the optimal configuration involved using a high-speed Phantom V341 camera with a Zeiss Makro-planar T*2/50mm ZF lens. For the first experiment the camera sensor was positioned at 1.4m, and a recording window of 2560x1100 px^2 was utilized. For the second experiment the camera was positioned at almost 2m from the tank.

To activate the camera, an auto-trigger functionality was employed. In the software Phantom camera control (PCC), the motion of the sphere or the cylinder was detected by scanning the pixel grey level variation across the entire auto-trigger region. Recording was triggered when a certain percentage of the total number of pixels inside the region was reached. The specific region positioning is illustrated in the figure below (2.16):

Figure 2-16 It is possible to see the auto-trigger box in the photo (the yellow one)

The auto-trigger window was placed in the front window, but it could have been placed in the window reflected in the mirror as well.

2.6. Calibration

Calibration is crucial for comparing data from the front view and the mirror view, especially for code validation and 3D trajectory ana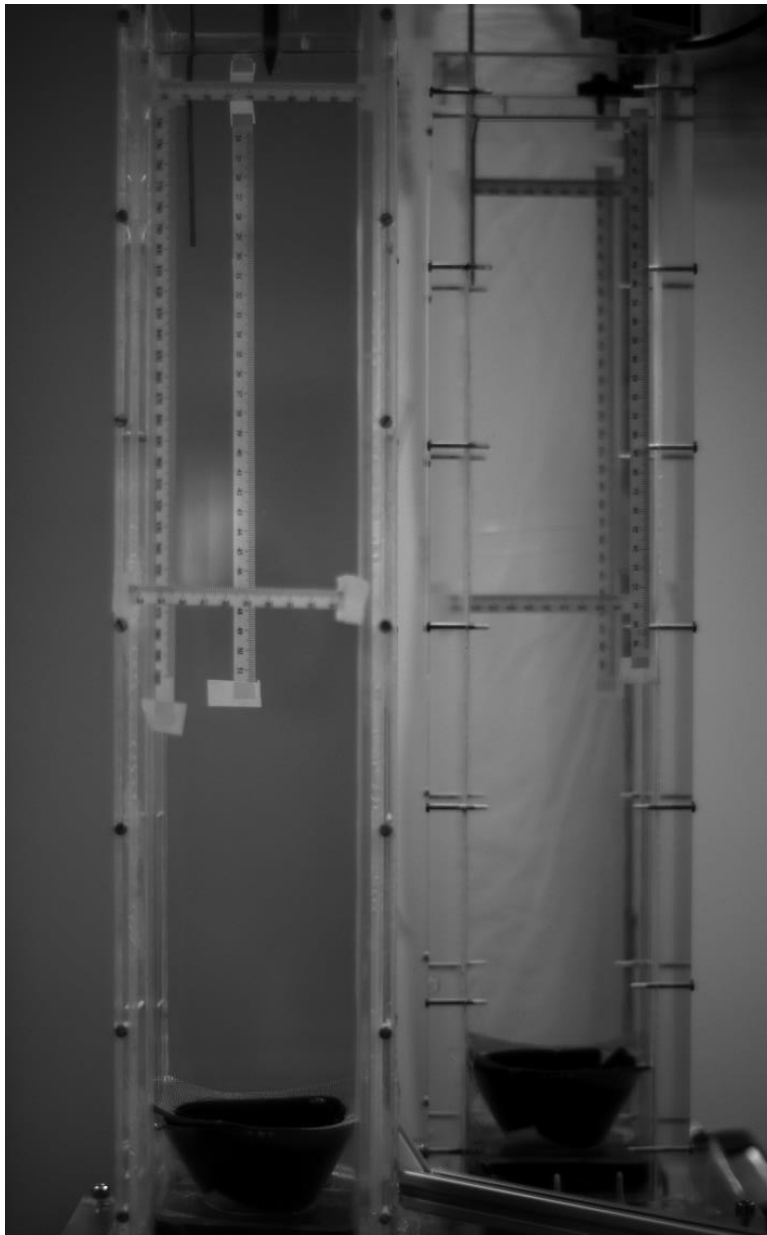lysis. The approach used by Castagna was deemed unsuitable for the new test bench experiment, which required a calibration target mounted on the rear part of the tank. This was because a motorized support for the checkerboard would be necessary.

Instead, a calibrated strip of paper, as shown in the figure, was utilized for calibration. The camera focus was directed to the rear part of the tank, providing the optimal solution between the view of the front and the mirror calibrated strip of paper. Subsequently, a calibration snapshot was taken, enabling the evaluation of the mm to px conversion factor using the ImageJ program. The calculation involved measuring the pixels corresponding to 0.05m in the upper and centre parts.

The problem with the method described above is the error introduced by reading the number of pixels, particularly in the mirror view, because the

Figure 2-17 Calibration image, characterized by the strip of paper on all the wall of the tank

strip is out of focus. To address this issue, the camera objective was changed from Zeiss Makro-planar T*2/50mm ZF lens to the 50mm ZF to obtain a better calibration snapshot, along with adjusting the aperture of the camera.

The calibration value for both views was chosen as the mean value between the values obtained from the front and rear parts of the tank since the falling occurred almost in the centre of the tank. This approach resulted in two different calibration values (for the upper and centre), allowing for the evaluation of distortion caused by the camera. The distortion value was computed based on the velocity using the formula below:

$$error = \frac{(v * factor_{upper-part} - v * factor_{centre-part})}{\left(v_{fin_{upperpart}} - v_{fin_{centrepart}}\right) \Big/ 2} * 100 \tag{2.6}$$

The velocity Z with the two calibrations for both the front and the mirror views was plotted in the images below. As is evident, the difference for the front view is lower than 0.25%, and for the mirror view, it is lower than 0.3%.

From figure 2.18 and 2.19, it is possible to derive that it is feasible to use just one calibration value for both the upper and centre parts.

The same analysis was done for the bigger tank, but also in that case the error between the two different calibration was very small so also in that case it was used just one calibration.
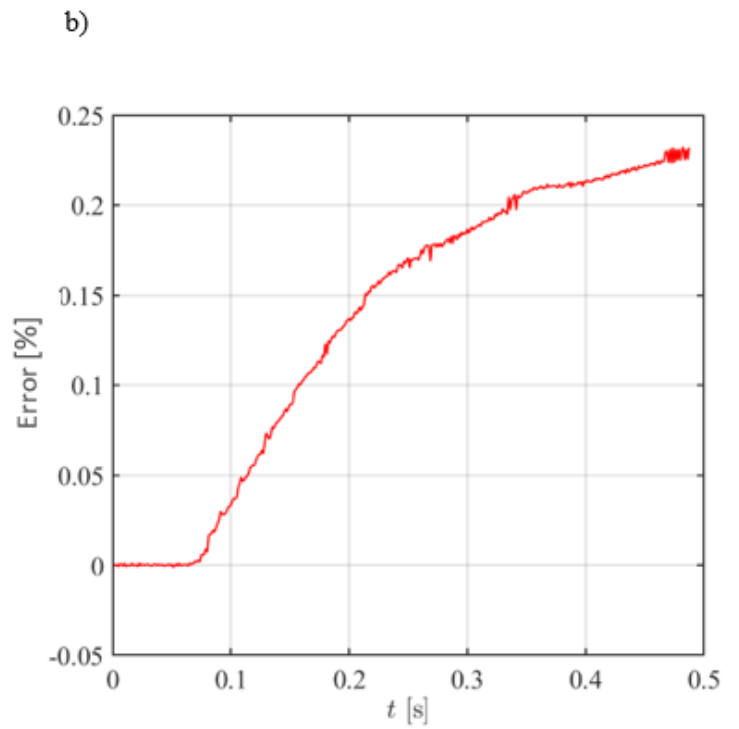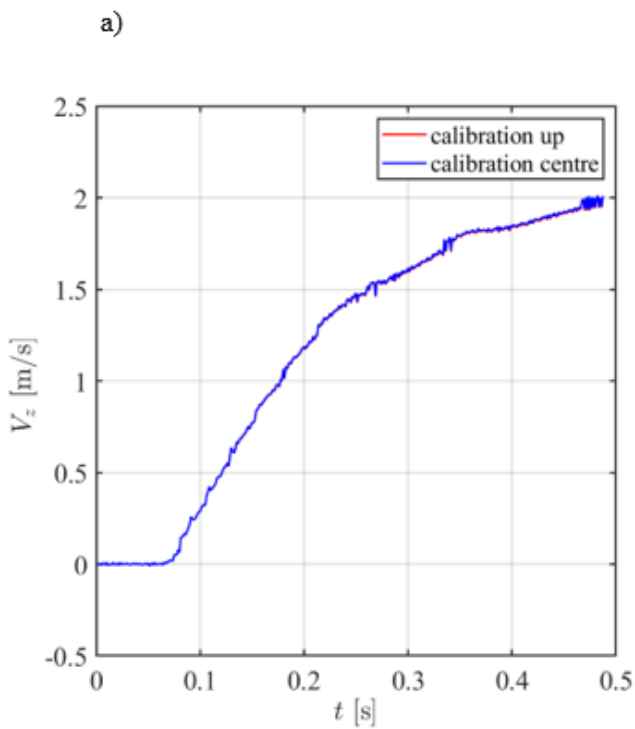
Figure 2-18 a) the representation of the velocity of a cylinder in the front face (L=27mm and D=10mm) with the two factor of conversion one based on the conversion in the centre of the tank and another in the upper part of the tank b) it represents the error between the two

Figure 2-19 a) the representation of the velocity of a cylinder in the mirror face (L=27mm and D=10mm) with the two factor of conversion one based on the conversion in the centre of the tank and another in the upper part of the tank b) it represents the error between the two
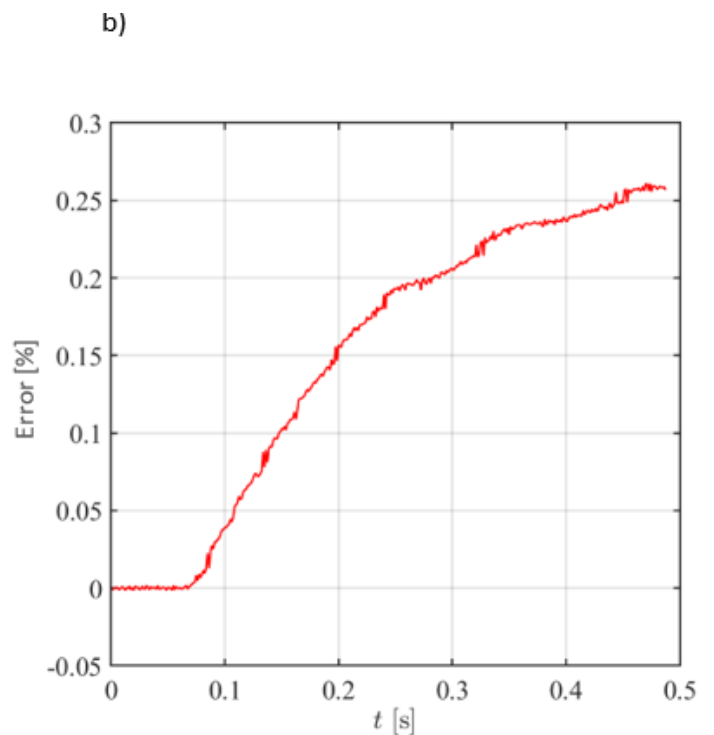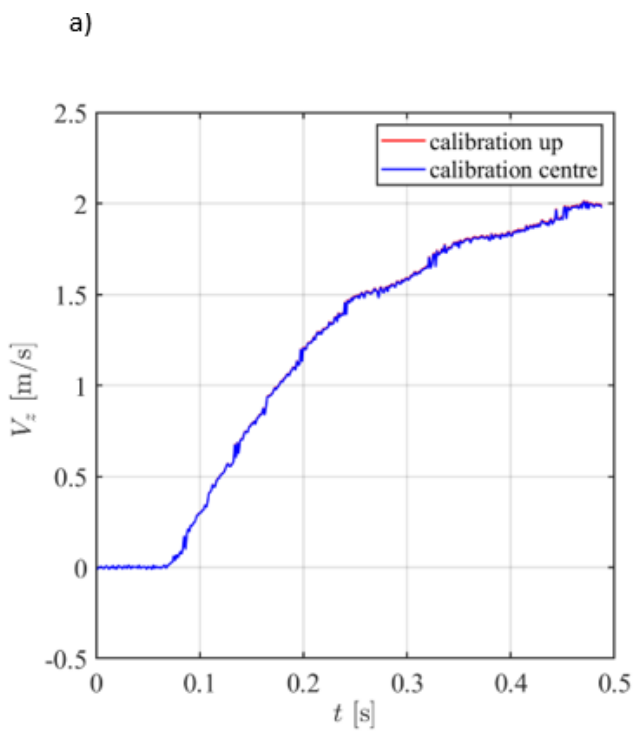
In addition, an attempt was made to use a variable calibration based on the position of the sphere/cylinder in the other window: the position of the mirror window was used to determine the exact position of the object on the Y-axis. Through a calculation, with calibration on both the front and rear faces of the tank, where the graduated paper strips were positioned, it should have been possible to achieve a more precise calibration. However, evaluating the error based on velocity, this was not feasible. This can be attributed to poor focus, leading to imprecise data readings. As we can see in the image below (Figure 2.20), while the error for the position for the constant calibration is at most around 5% of the diameter, in the case of variable calibration, it is higher, reaching up to 12%.
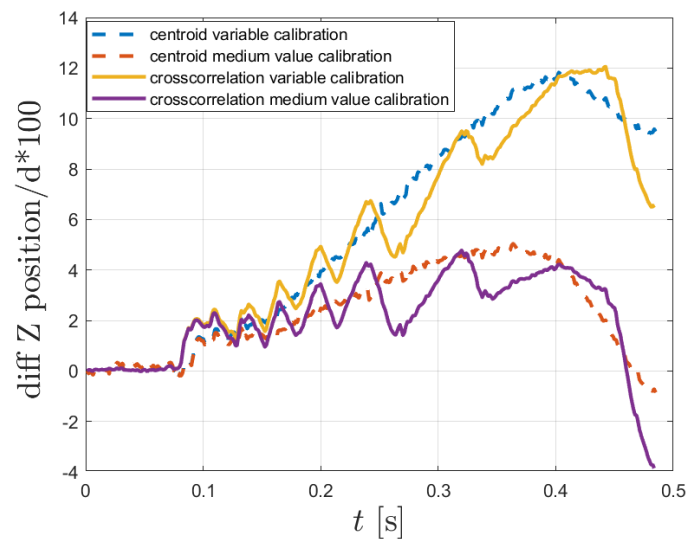

Figure 2-20 Different type of the calibration one based on the central value of the tank and the other a variable calibration based on the position of the other windows

In the case where the error in velocity is considered, we can observe that the difference between the two different type of calibration is very low, as we can see in figure 2.21
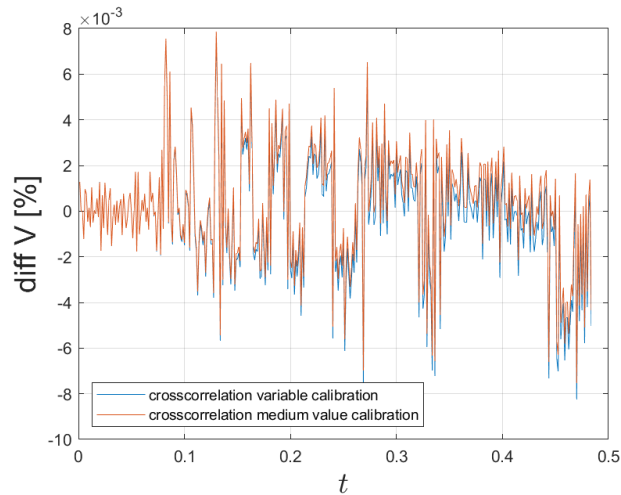
Figure 2-21 Error based on the different between the two velocities

From the results, given that no improvement was achieved with variable calibration, the choice has been made for constant calibration taken at the centre of the tank, where the sphere/cylinder is initially dropped.

2.7. Settling time

By reviewing the available literature on the subject, Horowitz and Williamson (2009) briefly discussed the topic, suggesting a settling time of two hours for a rising sphere and about one hour for a rising cylinder in pure water. They highlighted how disturbances in the fluid could lead to the appearance of random transverse motion.

Truscott [9] conducted additional experiments to justify the time suggested by Horowitz and Williamson (2009). A 2D two-component Particle Image Velocimetry (PIV) experiment was performed for each of the spheres. After an experimental run and resetting the sphere, PIV images were captured every 5 minutes for 1 hour. Results indicated that after 30 minutes, the measured PIV velocity closely matched the settling speed of the PIV particles. Therefore, a 30-minute wait time was chosen.

It's worth noting that these results are based on the ratio between the solid and fluid density, settled in the experiment at $\zeta=1.4$ for falling and $\zeta<1$ for a rising object. Intuitively, as ζ increases, the sensitivity of a falling sphere to residual disturbances decreases. Castagna (2019) used a settling time of 15 minutes, and the validity of this value was verified by comparing the results of tests executed with virtually infinite settling time (one night) with the same tests executed after 15 minutes.

So, based on what Castagna found, a 15-minute settling time was also used in the current case.

3. Experimental results

3.1. Post processing

For the processing it was use a code based on a cross-correlation technique which was practically implemented in MATLAB. The code was very useful for the calculation of the 3D time-resolved trajectory. For doing this, it was necessary to estimate the displacement of the sphere between two consecutive images.

3.1.1. Image pre-processing

The commencement of the procedural steps involved capturing a calibration image, necessitating a singular execution due to the absence of instrument movement throughout the entire experimental campaign. The calibration methodology was elucidated in detail in Chapter 2.6. Prior to the experiment's commencement, approximately 50-60 images were captured without the presence of the cylinder. This was done to establish an average background for both planes.

Following this initial phase, a video was generated, composed of discrete images. In each image, the delineation of the drop region was achievable for both the frontal and mirrored perspectives. The first step involved subtracting the background from each image, thereby reducing noise and eliminating fixed objects within the analysed field. Subsequently, the initial and terminal positions of the cylinder were identified within the images, facilitating the cropping of both the frontal and mirrored views.

In the lower segment of the tank, the region undergoing analysis underwent segmentation at a distance roughly equivalent to one diameter from the tank's bottom wall. This measure was implemented to mitigate potential end effects. Following this, two lateral limits were defined for both the mirrored and frontal images, effectively separating the two perspectives. It is then crucial to transition to a grayscale image where the images are converted to an intensity image in the range 0-255 and subsequently convert in an intensity equivalent value in the range 0-1. This operation allowed for the binarization of the images, using a threshold computed by Otsu method. The binarization allowed for the separation of the background from the cylinder.

After that the goal is to reduce the dimension of the image to a reduced windows approximately centred on the sphere. The computational cost of these operations was balanced by the savings in performing the cross-correlation operations on a small region of the whole image. For the evaluation of the centroids, it is used **'regionproprs'**, and the

value find for the MATLAB function it was used as centre of the windows. The windows could be rectangular or square.

This position of the centroid could be also use to detect a first trajectory of the sphere, also if this is less precise than the one from the cross correlation.

3.1.2. Cross-correlation

One of the most prevalent approaches for identifying the optimal match between two images involves employing local search techniques within a statistical framework. Let I_A and I_B denote the intensity fields of the interrogation windows on the first (F_A) and second (F_B) images, respectively. The cross-correlation describing their relationship can be formulated as follows:

$$R_{I_A I_B}(\Delta X_1 e_1 + \Delta X_2 e_2) = \sum_{i=-k}^{k}\left(\sum_{j=-L}^{L} I_A(i,j)I_B(i + \Delta X_1, j + \Delta X_2)\right) \qquad (3.1)$$

Here, 2K and 2L represent the dimensions of the interrogation windows in the e_1 and e_2 directions, respectively. For each potential shift, $\Delta X = \Delta X_1 e_1 + \Delta X_2 e_2$, the cross-correlation map is generated by evaluating the sum of the products of the overlapping pixels of I_A and I_B. The cross-correlation function quantifies the similarity between the two intensity fields, with the maximum $R_{I_A I_B}$ value indicating the optimal shift (ΔX) that best aligns with the particle displacement, denoted as 's.'

This method finds extensive application in Particle Image Velocimetry (PIV), where 's' corresponds to the mean motion of particles within the analysed interrogation window. This process is repeated for all interrogation windows to cover the entire analysed field. In the current study, a single interrogation window was chosen for each pair of analysed images, and binarized images were employed throughout.

Considering that the computational load for evaluating the cross-correlation function increases with the size of the interrogation window, practical cases may encounter computational limitations. Therefore, a more efficient method based on Fast Fourier Transform (FFT) is often employed in such instances:"

$$R_{I_A I_B} \leftrightarrow \widehat{I_A} * \widehat{I_B^*} \qquad (3.2)$$

$((.)^*$ is the symbol of the complex conjugate)

In the given context, a 2D Fast Fourier Transform (FFT) is indispensable. After multiplying the coefficients of the first image with the complex conjugates of the coefficients of the

second image, the inverse Fourier transform is applied to obtain the cross-correlation value. This comprehensive procedure was conducted utilizing the '**xcorr2'** function implemented in MATLAB.

A limitation of this function is that the shift s could be only represented by integer pixel value, for this reason it was introduced a subpixel cross-corelation. This is a method to increase the spatial resolution and consists in a fit of the correlation data to a gaussian function. In this case the sub-pixel correlation was made before for the x-axis and then for the y-axis, combining the results it is possible to obtain a 2D subpixel correlation. For the gaussian it was used five points around the maximum value of the cross correlation. In this way it is possible to obtain a more precise position of the cylinder.

 It was found a problem: it is difficult to detect the x-moviment of the cylinder due to the disk and the reflection of the light on it that create a false lateral edge for the cylinder. To solve this problem, I try to change the threshold used (otsu methods) and see what append to the cylinder, in particular this analysis is based on the variation of the diameter, because we don't want that this variation increases because it could cause problem in the cross correlation. In particular, the otsu threshold is 0.54 and with this threshold the cylinder obtain is the one shown in figure3.1 and the variation of the diameter is the one in figure3.3. As we can see the variation of the diameter is about 60±1 px.

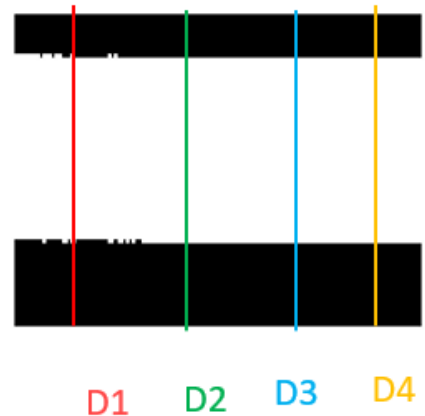*Figure 3-1 Variation of the diameter with the Otsu threshold*

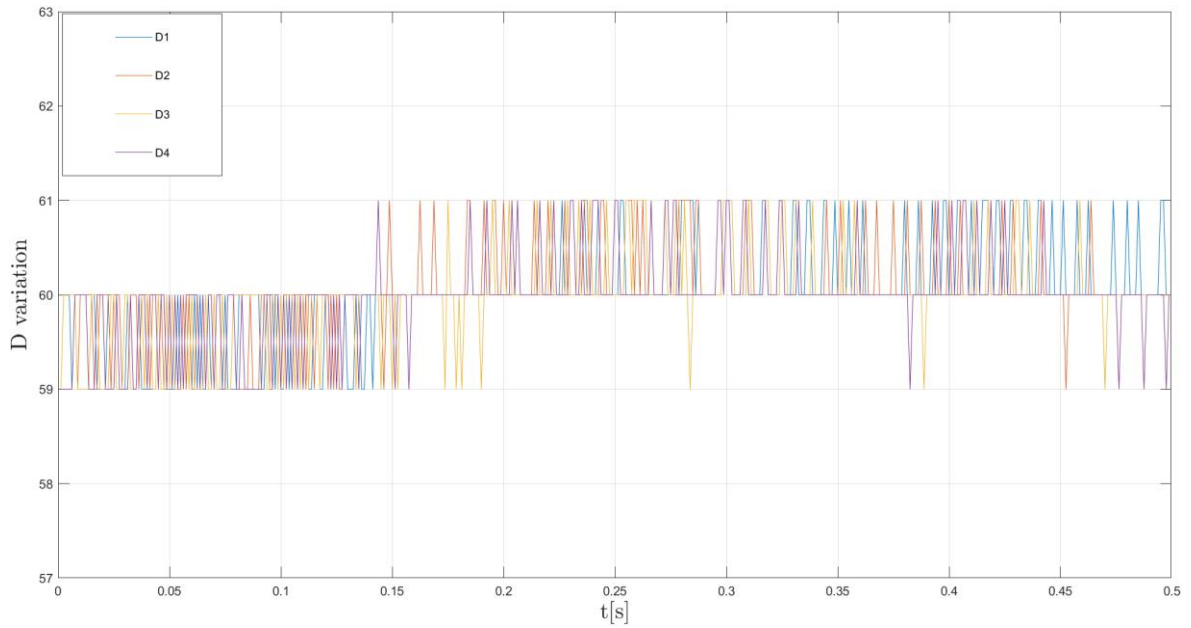*Figure 3-2 different diameter considered*

Figure 3-3 Variation of the cylinder diameter

Changing the threshold decreasing it as we can see the disk are highlight more than before and also there is a big variation of the diameter increasing it, we saw that the disk start to disappear but at the same time the variation of the diameter bigger than the one with the first threshold, as we can see in the figure below (3.4)
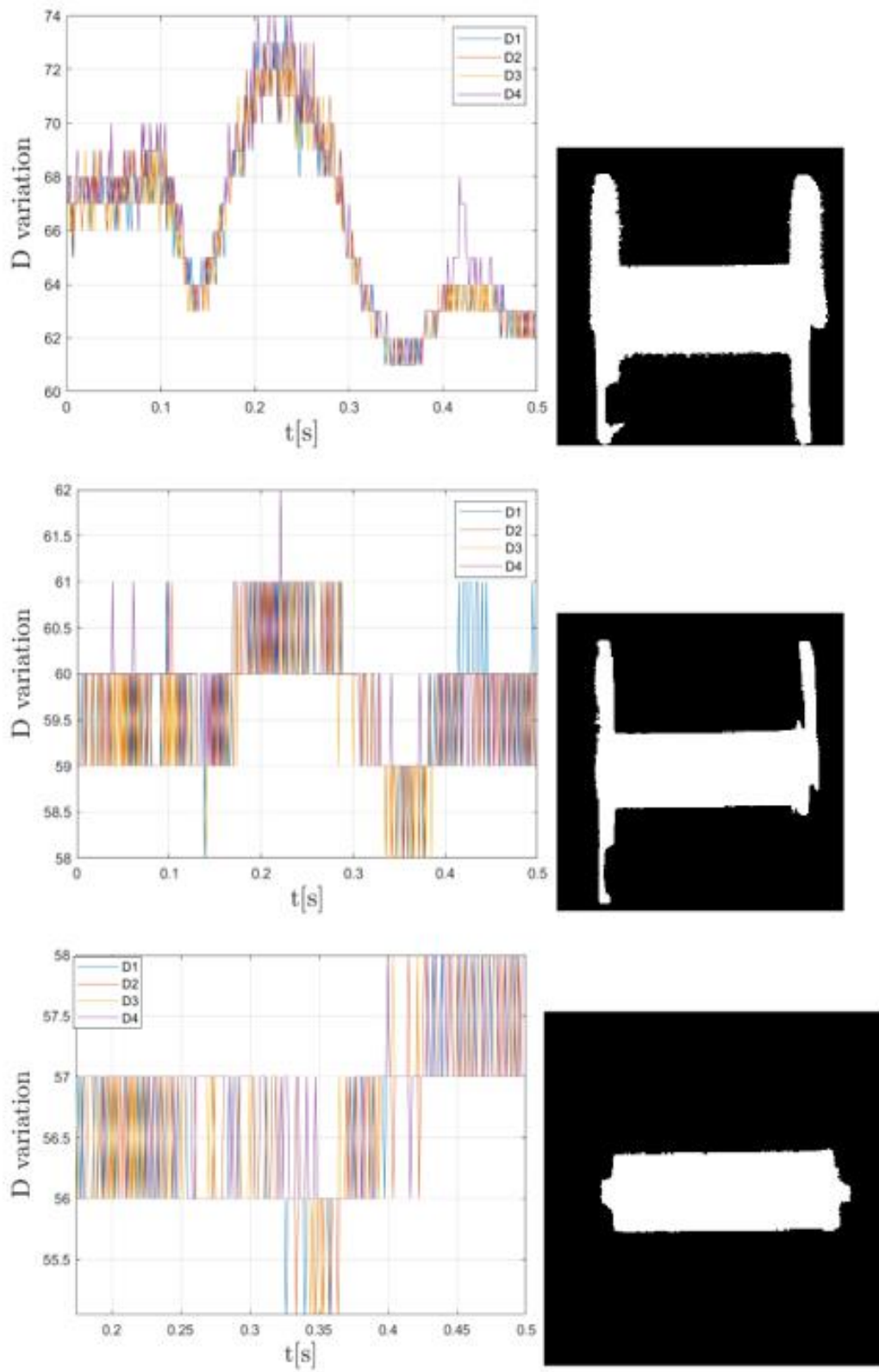
Figure 3-4 Variation of the cylinder with three different threshold 0.4, 0.6 and 0.8

So, at the end, in the first analysis the x-movement of the cylinder is not considered, also because we are more interested in the z-movement.

3.1.3. Validation of the code

To ensure the efficacy of the code, a validation process is imperative. This involves comparing the Z velocity between the front and mirror views. The validation is made on the velocity because it is the parameter of interest to compute the drag of the cylinder. To achieve this, a conversion from pixels to meters was conducted for both perspectives, utilizing distinct conversion factors. Subsequently, the results were juxtaposed to ascertain the consistency of the outcomes. This process was made for both the sphere to compare with the result obtain from Castagna (2019) and also for the cylinder.

- *Validation for the sphere*

In Figure 3.5, the velocity error is depicted. As observed, the maximum error is less than 0.01% with a mean value of it around 0. A similar value it was find also from Castagna. The error assessment is conducted as follows:

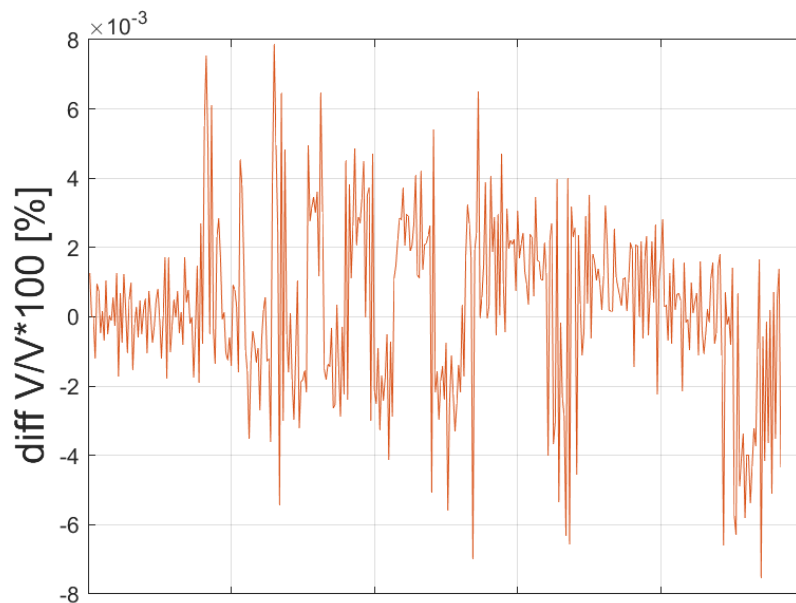$$error = \frac{V_{front} - V_{mirror}}{\bar{V}} * 100 \qquad (3.3)$$

Figure 3-5 Evaluation of the error between the two Z velocity from the mirror and the front view of a sphere of diameter of 15mm

Therefore, we can consider the code validated for the sphere. However, to ensure its compatibility with the cylinder, similar validation procedures were applied.

- *Validation for the cylinder*

As evident in the image below (Figure (3.6)), the errors in this case are higher compared to those observed for the sphere but remain below 0.015%. Consequently, the code can be considered validated for the cylinder as well.
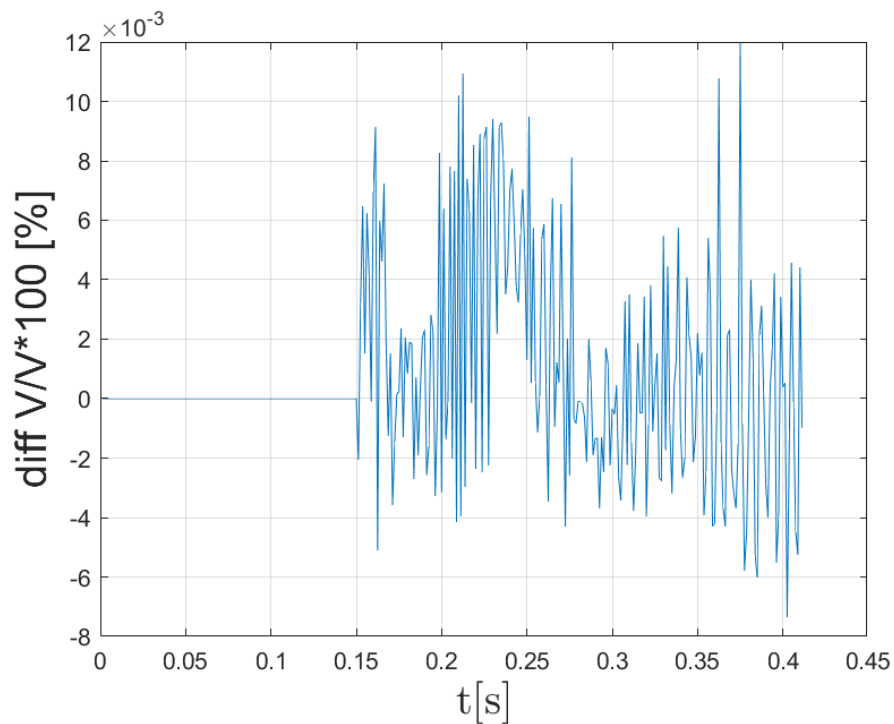

Figure 3-6 Evaluation of the error between the two Z velocity from the mirror and the front view of a cylinder of dimensions D=10mm and L=27mm

3.2. Experimental results smooth normal cylinder

Figure 3-7 Different images during the falling of the cylinder

In the figure below (figure 3.7), various images from the experiment conducted during the post-processing for the cylinder are depicted. We will now delve into the analysis of some results obtained from the experiment.

The initial parameter under consideration is associated with the cylinder described in Table 2.1, which proves highly useful for constructing the MATLAB code. The primary focus is on the velocity, directly evaluated through cross-correlation. The initial signal obtained exhibited some noise; therefore, instead considered all the photo it was considered just one photo over 5 because the moving average of five point applied by the MATLAB function does not give nice results.

It was crucial to compare the experimentally obtained velocity with a velocity termed "theoretical" in this paper, derived from a MATLAB code through an iterative cycle utilizing the curve in Figure 1.14.

In the subsequent figures (Figure 3.8 and 3.9), the three different z-velocities are presented: one from the front view, another from the mirror views, and the third from the MATLAB code. Observable agreement exists among the various curves in the final segment when the final velocity is reached, though not in the initial part. This phenomenon may be attributed to the friction between the disk and the support system. While an alternative release system could be considered, it was not implemented in this thesis.

Furthermore, a correlation is noted between the increase in weight and an augmentation in velocity, as both the Archimedes force and the drag force increase. However, these forces prove insufficient to counterbalance the heightened weight. Additionally, it is noteworthy that the cylinders almost reach the final velocity simultaneously, yet the descent of the second cylinder (Figure 3.9) had a shorter duration.
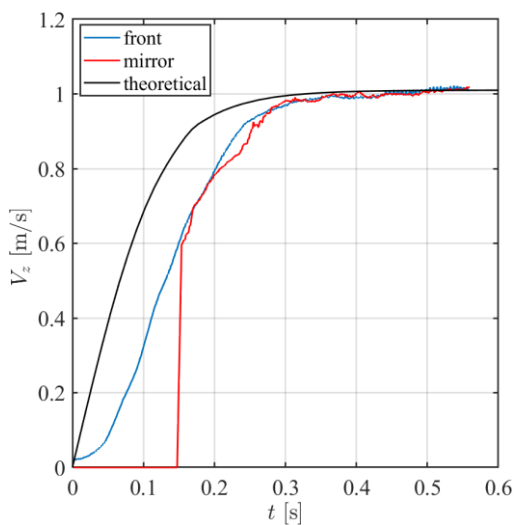

Figure 3-8 velocity over time for the cylinder of D=10mm and L=27mm

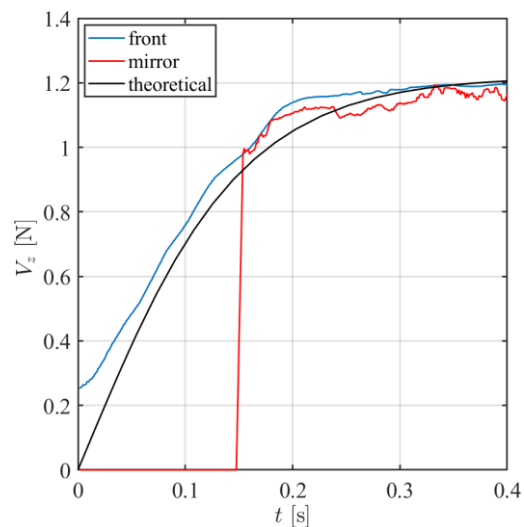Figure 3-9 velocity over time for the cylinder of D=16mm and L=67mm

From the velocity, it is now possible to derive the acceleration over time by taking the derivative. This acceleration value will initially be higher and then tend towards zero. With these data, we have all the necessary information for evaluating the drag coefficient (utilizing the data from Equation 2.3).

In this case as well, a similar trend in the velocity curves is evident. Specifically, a concordance is observable only when the final velocity is reached (at approximately 0.35 seconds). The calculated value of Cd is found to be 1.079 for the smaller one and 1.081 for the larger cylinder.

The mirror trajectory is also noteworthy; indeed, an oscillatory behaviour is observable, as depicted in Figures 3.6 and 3.7.
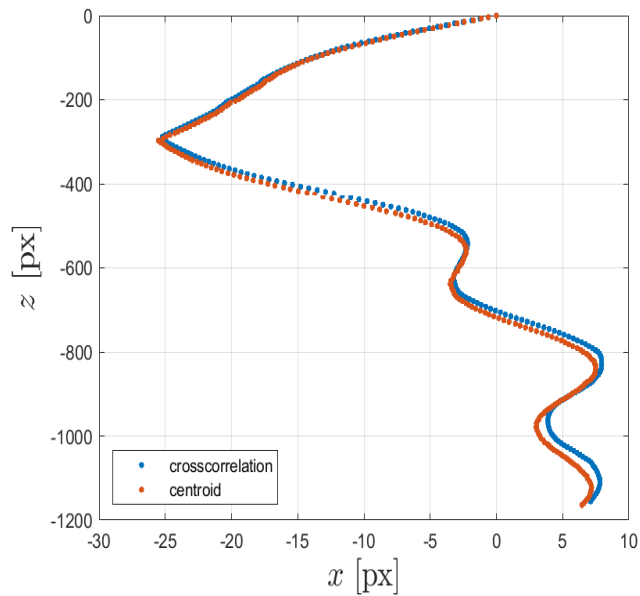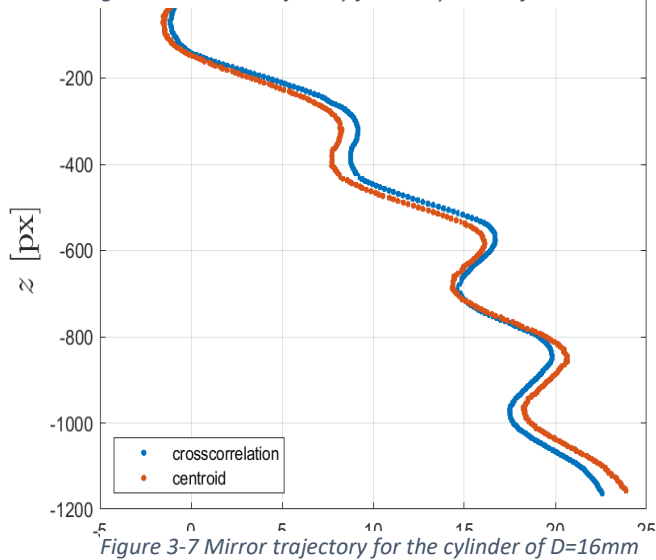

Figure 3-6 Mirror trajectory for the cylinder of D= 10mm

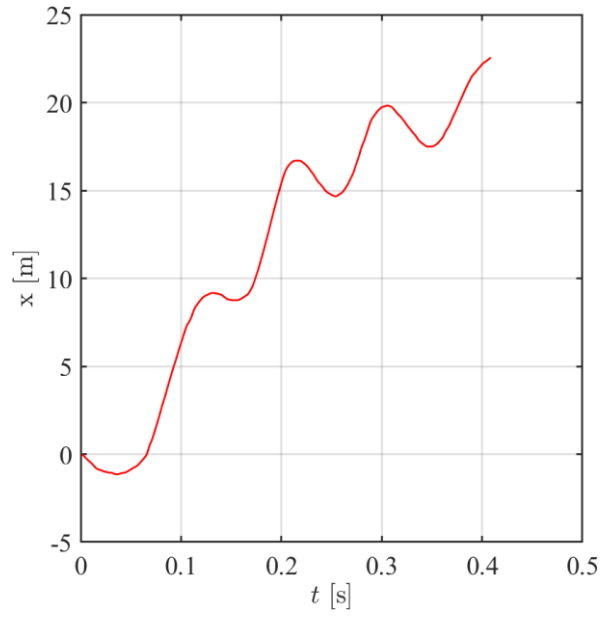Figure 3-7 Mirror trajectory for the cylinder of D=16mm

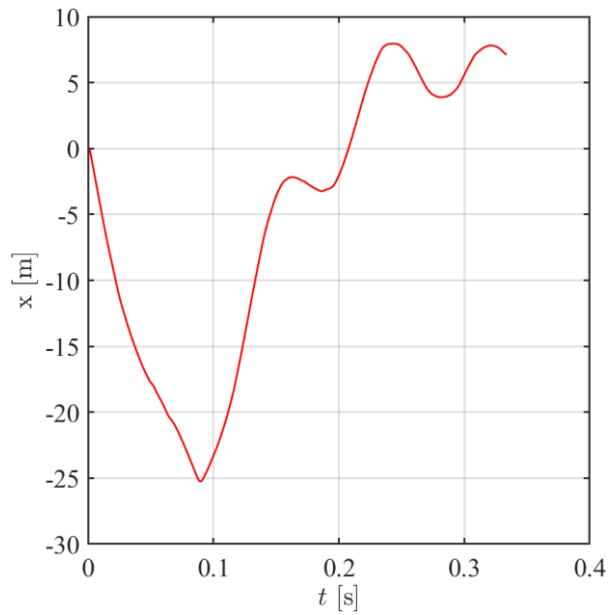*Figure 3-8 Y-trajectory over time for the cylinder of D=10*

Figure 3-9 Y-trajectory over time for the cylinder of D=16

In this scenario, it is believed that this trend is attributed to the release of vortices during the fall. To characterize this behaviour, the Strouhal number was evaluated, calculated as:

$$St = \frac{fD}{v}$$

(3.4)

To ascertain the oscillation frequency, the Fast Fourier Transform was applied, yielding the characteristic frequency value. The calculation of the Strouhal number was then derived from this value. For the first case, a value of 0.11 was determined for the smaller cylinder, and a value of 0.13 for the larger one.

All of this analysis is crucial for the development of the MATLAB code. We can now transition to the discussion of the superhydrophobic surface and the smooth cylinder of the same dimensions used as a reference case.

3.3.   Results of superhydrophobic cylinder

Now, we are going to analysed the seven different cylinders described in Table 2.2. The initial step is the analysis of the reference case. As depicted in the figure below (3.10), the velocity is observable.
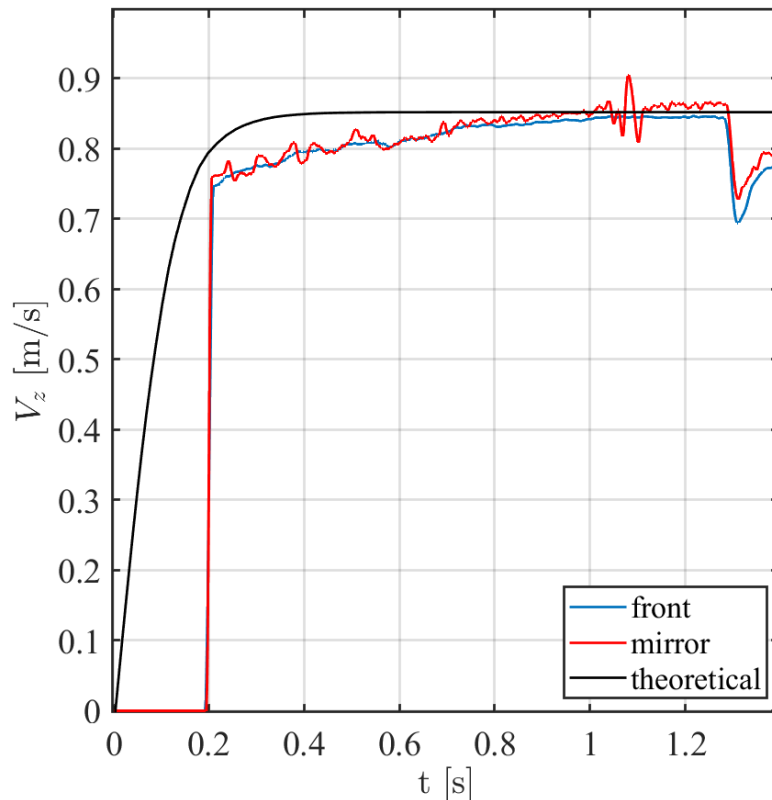

Figure 3-10 Z-velocity over time for the smooth cylinder (reference case)

The final velocity is reached at 0.9 seconds, which is later than the predicted case, but the final velocity aligns with expectations. In the last segment, the effect of the wall is noticeable.

When the velocity decreases, it is because the cylinder is very close to the wall, but since it is at the end of the tank, this proximity is not a concern.

The next step involves analysing the cylinder without coating, specifically focusing on cylinders 6 and 7 from Table 2.2. These cylinders are more influenced by the superhydrophobic surface. In this case, a perfectly linear drop is observed. Notably, there is a peculiar trend compared to the previous velocity results.
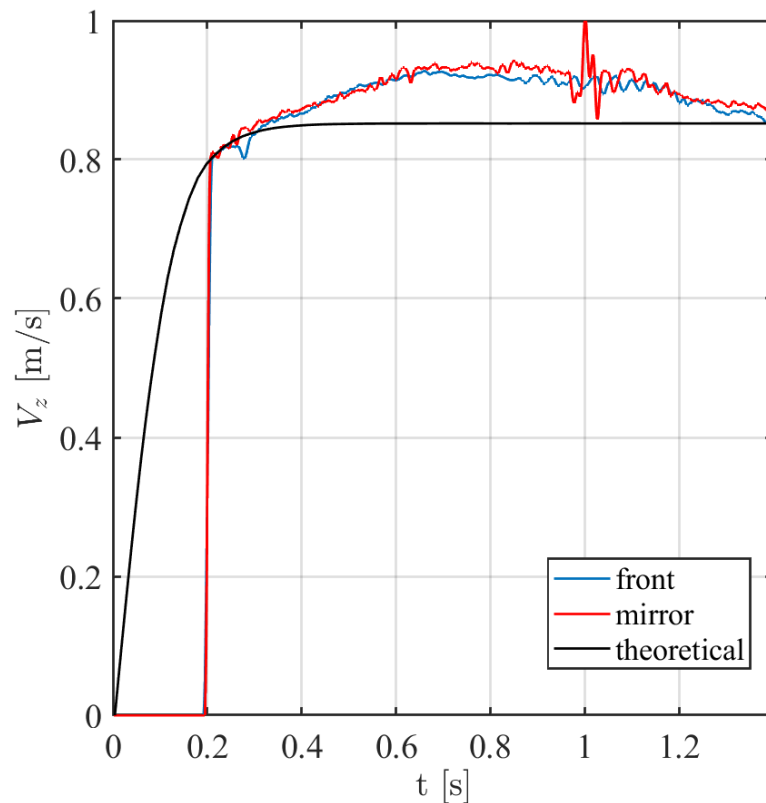

Figure 3-11 Z-velocity over time for the roughness cylinder without coating (cylinder 7)

As evident, before reaching the final velocity, the cylinders attained a higher velocity, followed by a subsequent decrease. This phenomenon could be attributed to small air bubbles trapped within the surface roughness. During the fall, these bubbles initially create a slip velocity. However, due to the high velocity attained during the descent, the bubbles eventually detach from the cylinder, resulting in a reduction of velocity. This trend is unique to this particular cylinder and is not observed in the other two without coating. This events could cause problem during the evaluation of the drag in fact the drag will be in this case lower than the real value.

The last cylinder under analysis is the coated cylinder. As anticipated, the velocity in this case is higher than the reference case, attributable to the lower drag compared to the reference case.

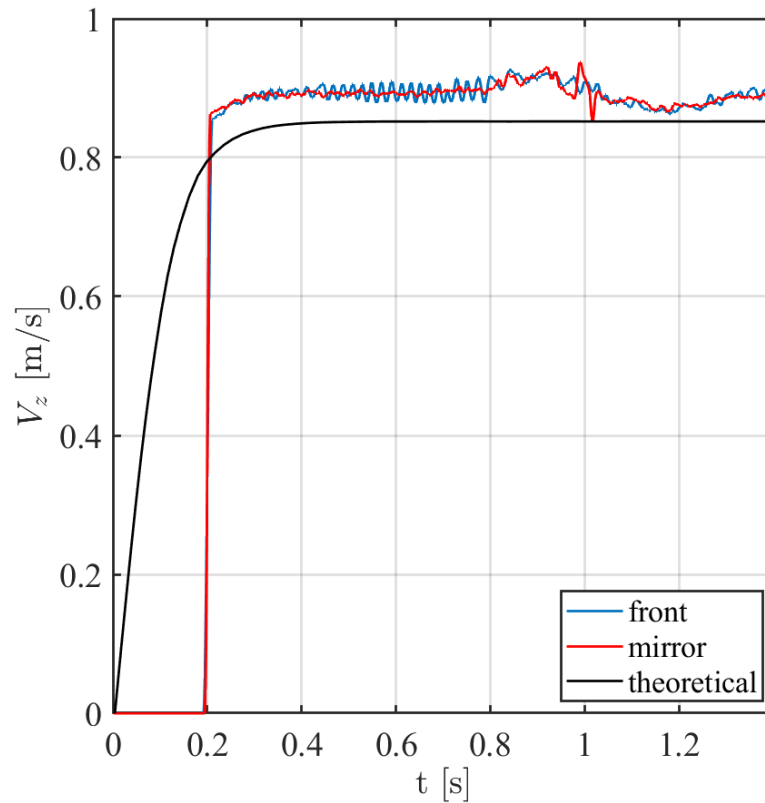*Figure 3-12 Z-velocity over time for the roughness cylinder with coating (cylinder 6)*

Now, following the evaluation of velocity, it is possible to assess the drag coefficient, a key parameter of interest. The initial data analysis indicates a reduction in drag due to the superhydrophobic surface. However, it is crucial to quantify this reduction precisely. So we are going to analysed the different value of C_d in the tab.3.1.

	Cylinder 1	Cylinder 2	Cylinder 3	Cylinder 4	Cylinder 5	Cylinder 6	Cylinder 7
Cd	1.03	0.95	1.01	0.94	1.04	0.92	0.98
Drag reduction (ref)	_____	-8%	-2%	-9%	+1%	-11%	-4%
Drag reduction (same roughness)	_____	-6%	_____	-10%	_____	-6%	_____

Tab 3-1 Evaluation of the drag and its reduction

Now, an important task is to determine which parameters of the surface roughness have the most significant effect. Specifically, the first parameters under analysis are λ and h. From this point onward, the smooth cylinder will be represented in black, the cylinder with surface roughness but a normal surface in blue, and the cylinders
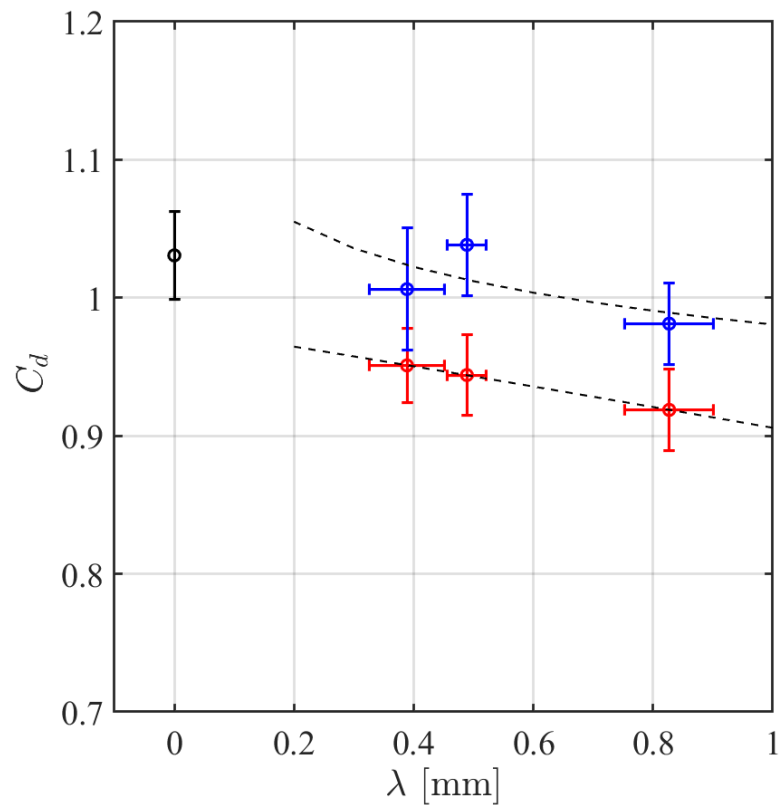with superhydrophobic surfaces in red.

Figure 3-12 λ over Cd for the 7 different cylinders

As observed in Figure 3.12, λ exhibits a tendency: an increase in λ corresponds to an increase in drag reduction. The drag reduction can be attributed to the increase in the length of the liquid-air interface (λ), resulting in a higher slip velocity. According to Samaha et al. (2011), a higher slip velocity corresponds to a more substantial reduction in drag. But it is important to pay attention because, this parameter is linked to the Cassie-Baxter state, associated with the maximum pressure supported by the interface (if λ increase the pressure supported by the interface decrease). Beyond this threshold, the interface transitions to the Wenzel state, resulting in a significant increase in drag. Therefore, it is crucial to find a compromise between drag reduction and the maximum pressure supported by the interface for the λ parameter.
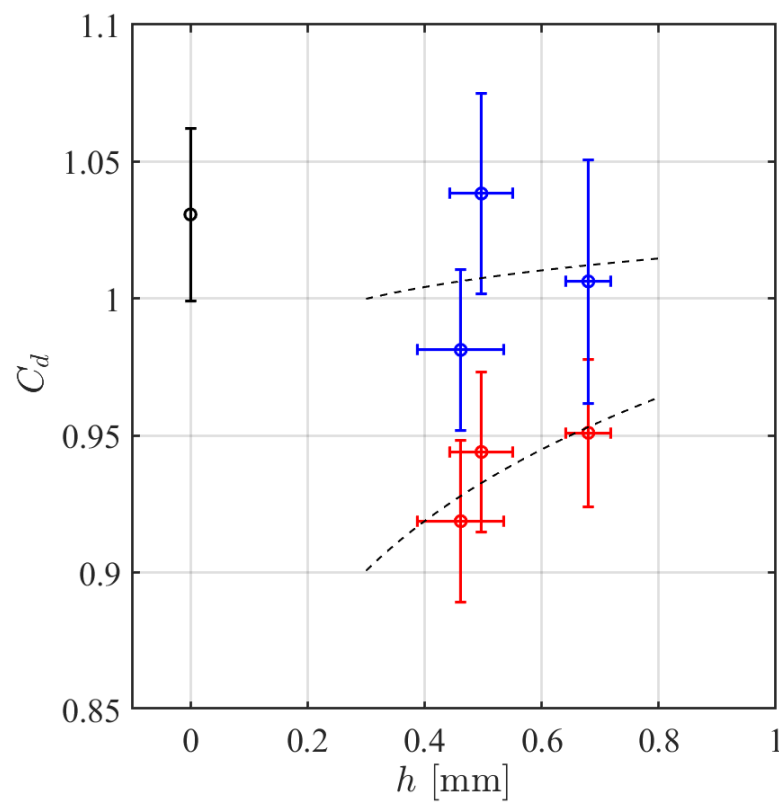

Figure 3-13 h over C_d for the 7 different cylinders

Regarding the parameter of height (Figure 3.13), it might appear to exhibit a trend, but in reality, the difference in height between the first two SH cylinder is approximately 0.03 mm, which is quite limited, especially considering the associated error. This difference is further overshadowed when compared to the disparity between the second and third cylinders. Examining the coefficient of resistance values reveals a significant difference for the first case, while the difference is not pronounced for the second case. Therefore, considering that height is not the only variable changing in this scenario, it is likely that height is not one of the primary influencing parameters. To confirm this, further experiments are necessary. In

particular, I believe that an important experiment could involve analyzing the drag coefficient of three cylinders with the same λ but different h.

In this way, it is possible to evaluate the impact solely of the parameter h (height), while concurrently examining whether the trapped air volume exerts an influence or remains inconsequential.

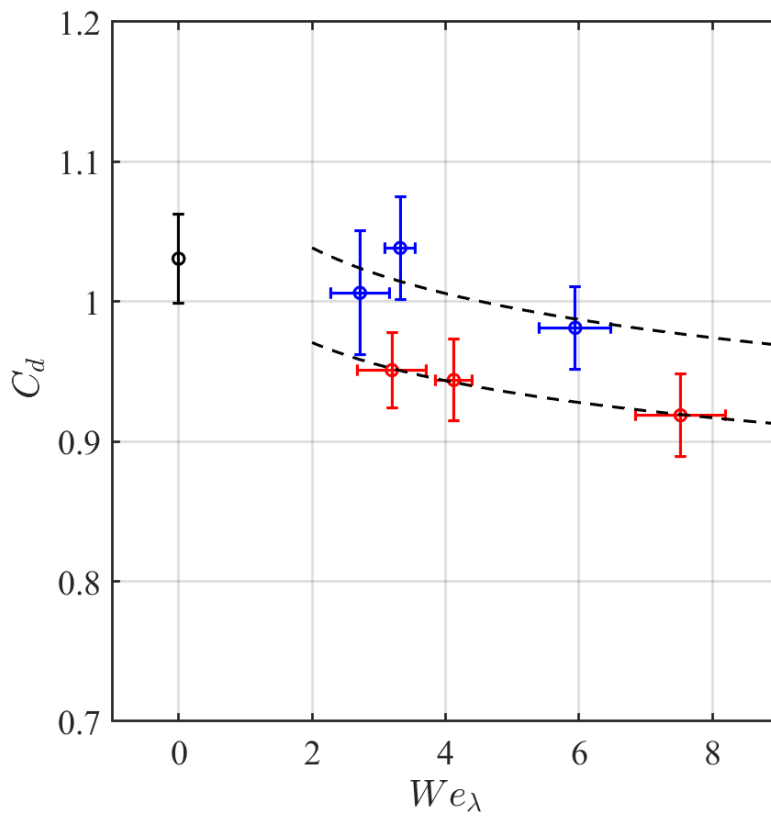Another parameter linked to λ, that for sure have an impact, is the Weber number.

Figure 3-14 Weber number over C_d for the 7 cylinders

The Weber number is determined based on the critical velocity, which corresponds to the final velocity. In this case as well, it is possible to observe almost the same trend for both the superhydrophobic (SH) cylinder and the normal one with roughness. According to Castagna, the critical value of Weber number is known to be 0.3, indicating the instability zone of the plastron. This instability is evident during the experiment, as shown in Figure 3.15. It could be of interest to further study the deformation of the plastron. Conducting additional experimental tests with a lighter material inside the cylinder may bring the Weber number closer to 0.3. Therefore, it is important to consider changing the steel rod inside the cylinder for such experiments.
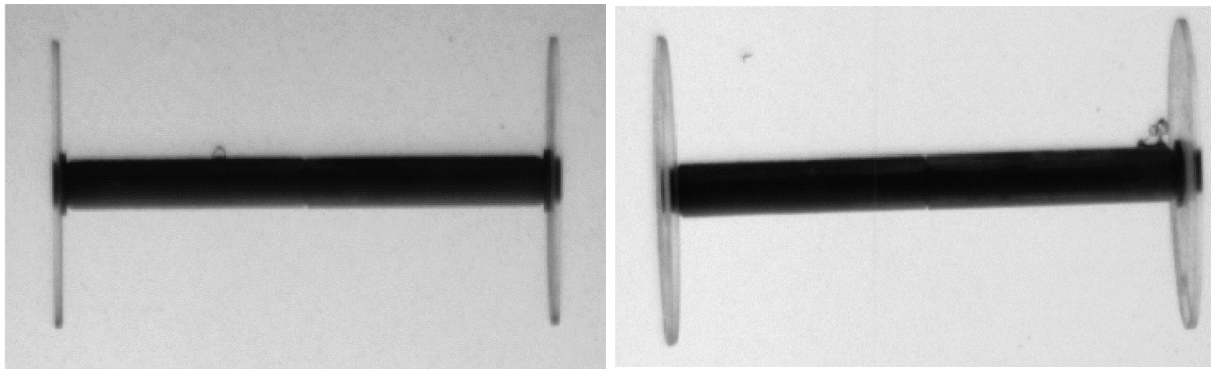

Figure 3-15 Deformation of the plastron

Another important nondimensional parameter is the ratio between λ and h (Figure 3-16). In this case, it is crucial to observe that as the ratio increases, there is a tendency for a decrease in the drag coefficient. I also considered in this case that the main influencing parameter is λ. This is supported by the fact that the second and third cylinders (red ones) have the same h but different λ compared to the first and second ones, where h has a significant variation compared to λ. From this, it can be deduced that the main parameter is consistently λ. However, to confirm this, it is important to conduct additional experiments with different types of roughness.
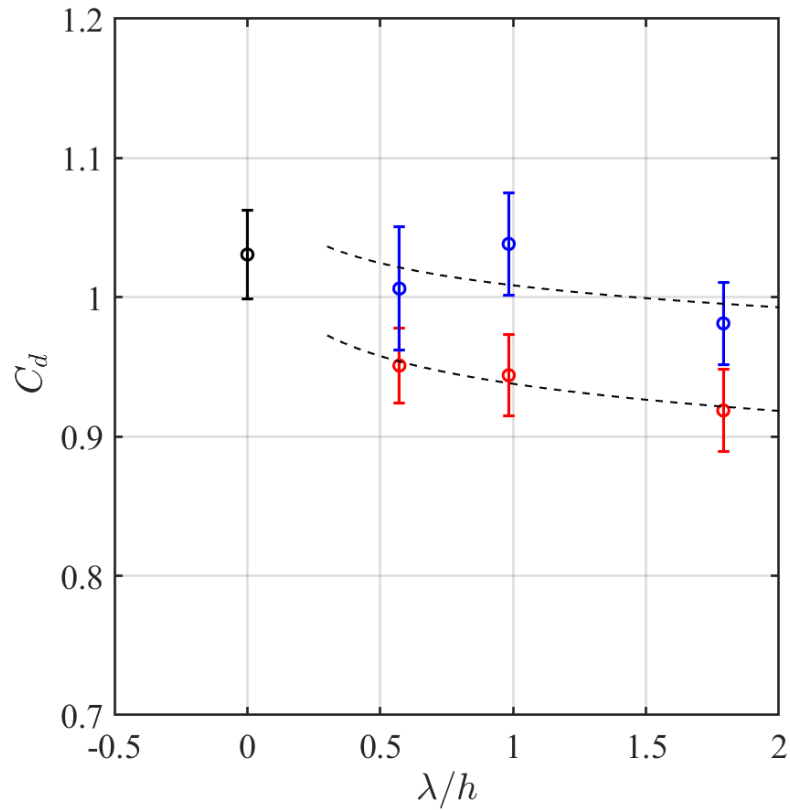
Figure 3-16 Ratio between the λ and the h over the drag coefficient

The last parameter analysed during this work is the gas fraction, defined as the ratio of the area of the air-water interface to the total surface area. This parameter is the main factor determining the static contact angle, which characterizes the hydrophobicity of the surface. Callies et al. (2005) experimentally demonstrated that as the gas fraction increases, the static contact angle also increases. Furthermore, the gas fraction has an impact on the slip length.

In this case, it is evident that as the gas fraction increases, the drag coefficient decreases, resulting in an increase in the liquid-air interface and subsequently, an increase in slip velocity and slip length.
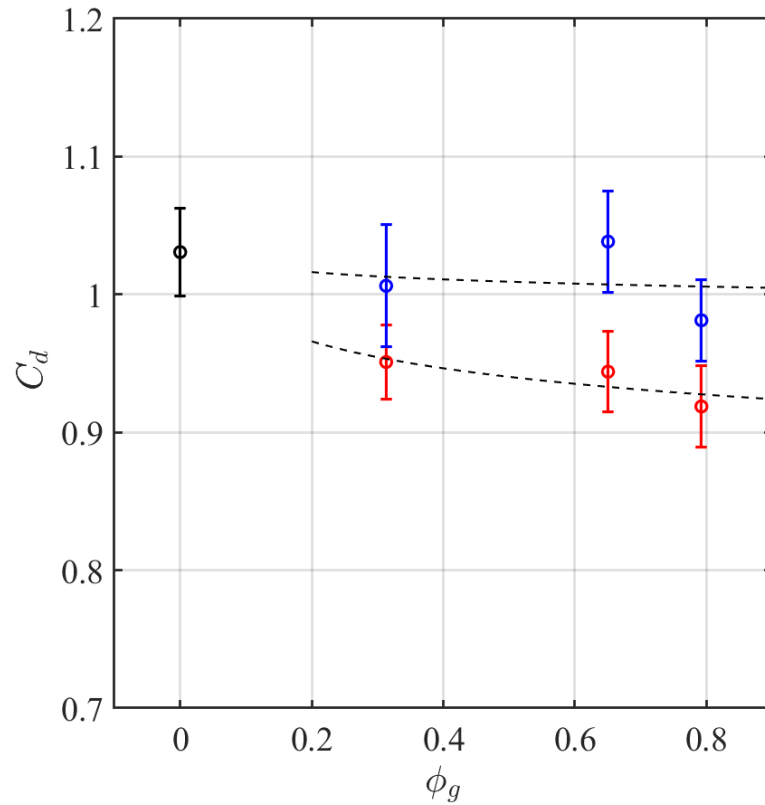
Figure 3-17 drag coefficient over the gas fraction

In this case, it is evident that the expected outcomes from the literature have manifested. However, certain studies highlight differences between interfaces with the same characteristics but varying parameters such as λ and w, corresponding to the stream and spanwise directions, and these differences directly influence the gas fraction. In my experiments, these parameters are kept constant, so it could be interesting to vary their dimensions while maintaining the same area to observe the impact.

Another important aspect is the trajectory of the mirror view, already analysed for the first two cylinders. It is crucial to observe whether the same oscillation occurs in this case and whether the frequency of the oscillation is consistent across all cases or varies.

The first image we are going to analyze is the trajectory of the cylinder without coating. As we can see in all cases, the same type of oscillation is observable. If we compute the Strouhal number, it will be around 0.2 for all cases, consistent with the results of Muralidhar et al. (2011).

Figure 3-18 Mirror trajectory of the cylinder over time for the different cylinder without coating: a) smooth cylinder, b) cylinder 3, c) cylinder 5, d) cylinder 7

If we now analyse the results of the superhydrophobic cylinders:

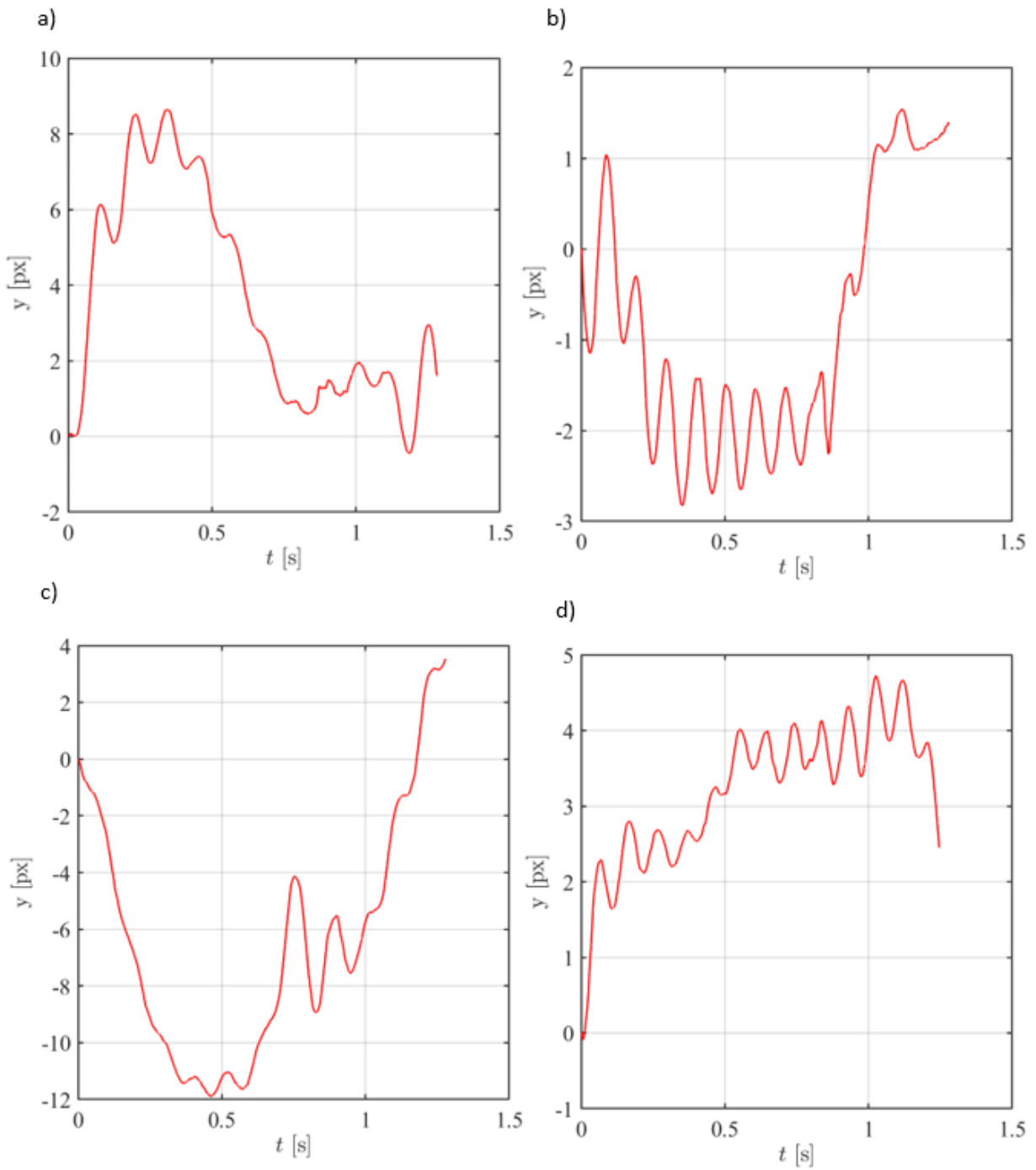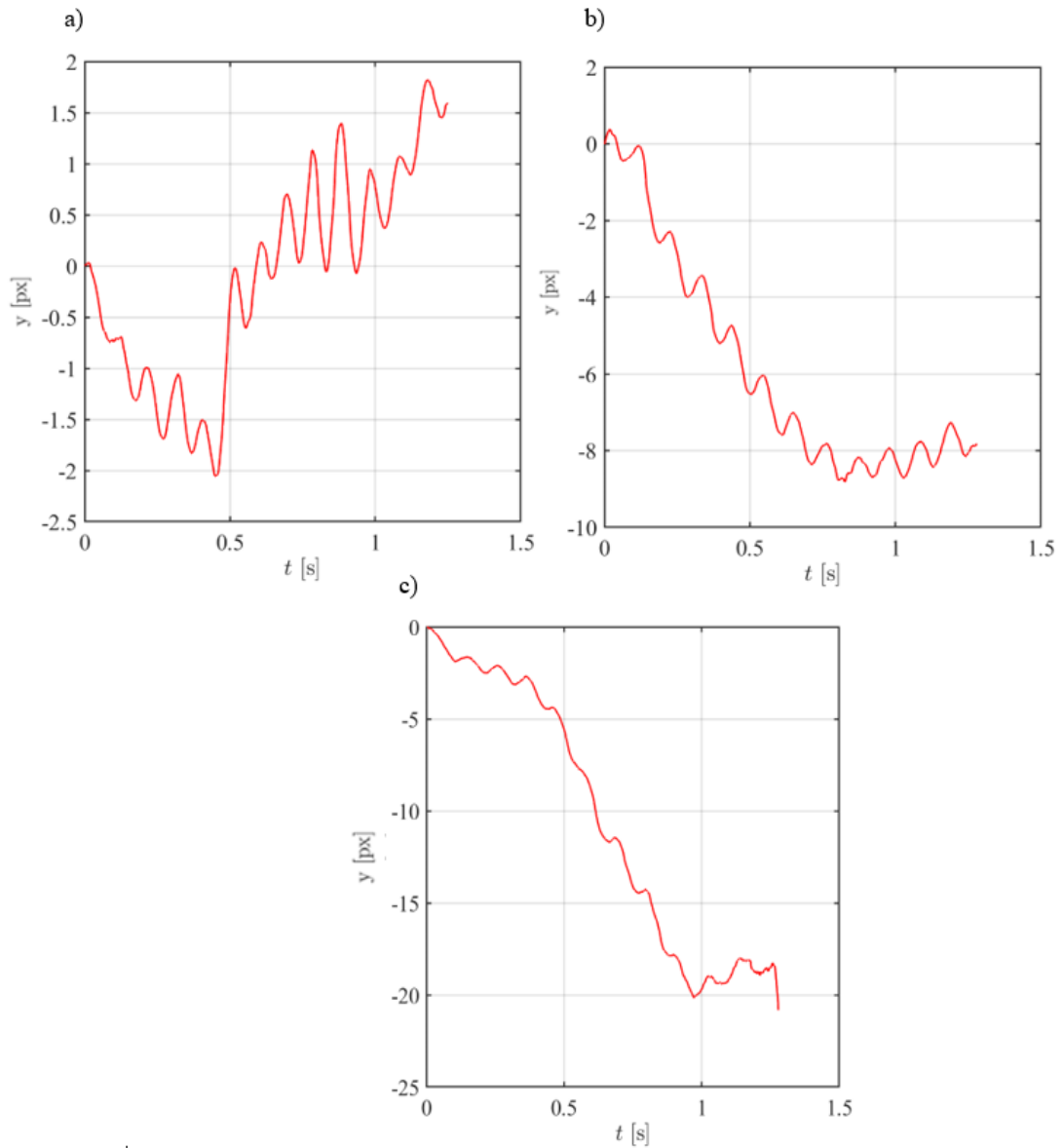*Figure 3-29 Mirror trajectory of the cylinder over time for the different cylinder with coating: a) cylinder 2, b) cylinder 4, c) cylinder 6*

In this case the Strouhal number is lower than the reference case in fact it is about 0.17-0.18. In this case there is a variation of frequency but also in velocity. There is no reference about the St number in the case of the superhydrophobic surface.

4. Conclusion

The primary objective of this work was to investigate the impact of superhydrophobic coating on drag, specifically whether it resulted in a tangible reduction at the laboratory scale and to quantify this reduction. This has significant implications in the context of marine surfaces, as these properties could lead to substantial friction reduction, translating to a practical reduction in fuel consumption—an increasingly important issue today.

This work builds upon research conducted by Marco Castagna in the same laboratory, but with the distinction that the bluff-body prototype used is a cylinder rather than a sphere. While there is limited literature available on this subject for cylinders, there is a substantial amount of experimental data accompanying this study.

During the experimental phase, the surface texture was generated using a 3D printer, and the main parameters were λ, w, and h. The superhydrophobic coating was applied using a spray coating method suitable for various applications.

The experimental tests involved the free fall of cylinders in water. Cylinders of the same mass with different roughness, both with and without coating, were tested, specifically using 3 different type of roughness. Post-processing of recorded drop videos was performed through in-house implemented codes, allowing the reconstruction of trajectory, velocity, and drag coefficient.

The experimental data revealed a reduction in drag, and it was observed that this reduction depended on the surface roughness parameters, with λ being identified as the main influencing parameter. Additionally, other parameters such as Weber number, gas fraction, and the ratio between the two roughness parameters (λ and h) showed correlation with the drag coefficient.

However, the analysis was conducted on only three cylinders, warranting an extension with additional cylinders. New experiments could involve cylinders with varying pillar heights but the same λ, allowing observation of the relationship between λ and h. This approach can help validate the assumption that h is not a primary parameter and may lead to a study of the trapped air volume inside the roughness and its effect on drag reduction. Another potential analysis involves varying the internal mass of the cylinder to alter the final velocity and Weber number, bringing closer alignment with the parameters tested by Castagna.

The last analysis focused on the mirror trajectory, exploring the oscillation movement and its connection to vortex release. The analysis of the Strouhal number revealed consistency with the results of other scientists for the reference case, and a lower value for the superhydrophobic coated cylinders.

An additional interesting phenomenon not analysed during this thesis is the study of plastron deformation. Observations from the videos during the falling phase suggest movement of the plastron, and further investigation with a different camera could provide valuable insights. This study is also connected to the reduction of drag, as plastron deformation could potentially lead to drag increase, making it an important aspect to analysed.

In conclusion, we can say that before the real-world application of this type of surfaces, many more years and extensive studies will be needed.

Reference

https://lambdageeks.com/pressure-drag/

C.L.M.H. Navier, Mémoire sur les lois du mouvement des fluides, Mem. Acad. R. Sci. Inst. France 6 (1823) 389–440

Rothstein, Jonathan P. "Slip on superhydrophobic surfaces." *Annual review of fluid mechanics* 42 (2010): 89-109.

C. Neinhuis, W. Barthlott, Characterization and distribution of water-repellent, self-cleaning plant surfaces, Ann. Bot. 79 (1997) 667–677.

K. Koch, B. Bhushan, Y.C. Jung, W. Barthlott, Fabrication of artificial Lotus leaves and significance of hierarchical structure for super hydrophobicity and low adhesion, Soft Matter 5 (2009) 1386–1393

http://www.hk-phy.org/atomic_world/lotus/lotus01_e.html.

M. Castagna, Contribution to the study and the modelling of the development of a boundary layer over a superhydrophobic surface: experimental and numerical coupled approach,2019

Bettaieb, Noura, et al. "Prediction of resistance induced by surface complexity in lubricating layers: Application to superhydrophobic surfaces." *Physical Review Fluids* 7.9 (2022): 094101.

Lauga, Eric, Michael P. Brenner, and Howard A. Stone. "Microfluidics: the no-slip boundary condition." *arXiv preprint cond-mat/0501557* (2005).

Vinogradova, Olga I. "Slippage of water over hydrophobic surfaces." *International journal of mineral processing* 56.1-4 (1999): 31-60.

Thompson, Peter A., and Sandra M. Troian. "A general boundary condition for liquid flow at solid surfaces." *nature* 389.6649 (1997): 360-362.

Barrat, Jean-Louis, and Lydéric Bocquet. "Large slip effect at a nonwetting fluid-solid interface." *Physical review letters* 82.23 (1999): 4671.

Choi C-H, Johan K, Westin A, Breuer KS. 2003. Apparent slip flows in hydrophilic and hydrophobic microchannels. Phys. Fluids 15:2897–902

Schnell E. 1956. Slippage of water over nonwettable surfaces. J. Appl. Phys. 27:1149–52

Baudry J, Charlaix E, Tonck A, Mazuyer D. 2001. Experimental evidence for a large slip effect at a nonwetting fluid-surface interface. Langmuir 17:5232–36

Cottin-Bizonne C, Cross B, Steinberger A, Charlaix E. 2005. Boundary slip on smooth hydrophobic surfaces: intrinsic effects and possible artifacts. Phys. Rev. Lett. 94:056102

Zhu Y, Granick S. 2001. Rate-dependent slip of Newtonian liquids at smooth surfaces. Phys. Rev. Lett. 87:096105

Zhu Y, Granick S. 2002. Limits of hydrodynamic no-slip boundary conditions. Phys. Rev. Lett. 88:106102

Cottin-Bizonne C, Cross B, Steinberger A, Charlaix E. 2005. Boundary slip on smooth hydrophobic surfaces: intrinsic effects and possible artifacts. Phys. Rev. Lett. 94:056102

Jin S, Huang P, Park J, Yoo JY, Breuer KS. 2004. Near-surface velocity using evanescent wave illumination. Exp. Fluids 37:825–33

Joly L, Ybert C, Bocquet L. 2006. Probing the nanohydrodynamics at liquid-solid interfaces using thermal motion. Phys. Rev. Lett. 96:046101

Joseph P, Tabeling P. 2005. Direct measurement of the apparent slip length. Phys. Rev. E 71:035303
Karniadakis G, Beskok A, Aluru N. 2005. Microfluids and Nanofluidics. New York: Springer

Pit R, Hervet H, Leger L. 1999. Friction and slip of a simple liquid at a solid surface. Tribol. Lett. 7:147–52

Samaha, Mohamed A., Hooman Vahedi Tafreshi, and Mohamed Gad-el-Hak. "Superhydrophobic surfaces: From the lotus leaf to the submarine." *Comptes Rendus Mécanique* 340.1-2 (2012): 18-34.

Bhushan, Bharat, and Yong Chae Jung. "Natural and biomimetic artificial surfaces for superhydrophobicity, self-cleaning, low adhesion, and drag reduction." *Progress in Materials Science* 56.1 (2011): 1-108.

Umgang mit Feuchtigkeit in Ansaugluftfiltrationssystemen | Nederman Mikropul

Cassie, A. B. D., and SJToTFS Baxter. "Wettability of porous surfaces." *Transactions of the Faraday society* 40 (1944): 546-551.

You, Donghyun, and Parviz Moin. "Effects of hydrophobic surfaces on the drag and lift of a circular cylinder." *Physics of Fluids* 19.8 (2007).

Legendre, Dominique, Eric Lauga, and Jacques Magnaudet. "Influence of slip on the dynamics of two-dimensional wakes." *Journal of fluid mechanics* 633 (2009): 437-447.

Muralidhar, Pranesh, et al. "Influence of slip on the flow past superhydrophobic circular cylinders." *Journal of Fluid Mechanics* 680 (2011): 459-476.

Brennan, J. C., et al. "Investigation of the drag reducing effect of hydrophobized sand on cylinders." *Journal of Physics D: Applied Physics* 47.20 (2014): 205302.

Kim, Nayoung, Hyunseok Kim, and Hyungmin Park. "An experimental study on the effects of rough hydrophobic surfaces on the flow around a circular cylinder." *Physics of Fluids* 27.8 (2015).

Williamson, C. H. K. "Three-dimensional wake transition." *Journal of Fluid Mechanics* 328 (1996): 345-407.

Bruschi, Giancarlo, et al. "Drag coefficient of a cylinder." *University of California, San Diego* (2003).

Williamson CHK, Wu J, Sheridan J. 1995. Scaling of streamwise vortices in wakes. Phys. Fluids. In press

Williamson CHK. 1988a. Defining a universal and continuous Strouhal-Reynolds number relationship for the laminar vortex shedding of a circular cylinder. Phys. Fluids 31:2742

Williamson CHK. 1988b. The existence of two stages in the transition to threedimensionality of a cylinder wake. Phys. Fluids 31:3165

Bang H, Fey U, Noack BR, Konig M, Eckel- mann H. 1995. On the transition of the cylinder wake. Phys. Fluids 7:1

Williamson CHK. 1995a. Three-dimensional wake transition behind a cylinder. J. Fluid Mech. Submitted

Williamson CHK. 1995b. Vortex dynamics in the wake of a cylinder. In Vortices, ed. S Green, Chapter 5. Dordrecht: Kluwer

Williamson CHK. 1992a. The natural and forced formation of spot-like dislocations in the transition of a wake. J. Fluid Mech. 243:393

Williamson CHK. 1992b. Wave interactions in the far wake. See Eckelmann et al 1992, pp. 333-37

Una1 MF, Rockwell D. 1988. On vortex shedding from a cylinder: Part 1. The initial instability. J. Fluid Mech. 190:491

Schiller L, Linke W. 1933. Druck und Reibungswiderstand des Zylinders bei Reynoldsaachen Zahlen 5,000 bis 40,000. Z. Flugtech. Motorluft. 24:193

Roshko A. 1993. Perspectives on bluff body aerodynamics. J. Wind Ind. Aerodyn. 49:79

Horowitz, M., and C. H. K. Williamson. "Vortex-induced vibration of a rising and falling cylinder." *Journal of Fluid Mechanics* 662 (2010): 352-383.